

**Title: Disk tearing in a young triple star system with misaligned disk/orbit planes**

**One sentence summary:** We observe disk tearing in a triple star system, where gravitational torques have warped the disk and broken the inner disk into an eccentric ring.

**Authors:** Stefan Kraus,<sup>1\*</sup> Alexander Kreplin,<sup>1</sup> Alison K. Young,<sup>1,2</sup> Matthew R. Bate,<sup>1</sup> John D. Monnier,<sup>3</sup> Tim J. Harries,<sup>1</sup> Henning Avenhaus, Jacques Kluska,<sup>1,4</sup> Anna S. E. Laws,<sup>1</sup> Evan A. Rich,<sup>3</sup> Matthew Willson,<sup>1,5</sup> Alicia N. Aarnio,<sup>6</sup> Fred C. Adams,<sup>3</sup> Sean M. Andrews,<sup>7</sup> Narsireddy Anugu,<sup>1,3,8</sup> Jaehan Bae,<sup>3,9</sup> Theo ten Brummelaar,<sup>10</sup> Nuria Calvet,<sup>3</sup> Michel Curé,<sup>11</sup> Claire L. Davies,<sup>1</sup> Jacob Ennis,<sup>3</sup> Catherine Espaillat,<sup>3,12</sup> Tyler Gardner,<sup>3</sup> Lee Hartmann,<sup>3</sup> Sasha Hinkley,<sup>1</sup> Aaron Labdon,<sup>1</sup> Cyprien Lanthermann,<sup>13</sup> Jean-Baptiste LeBouquin,<sup>3,13</sup> Gail H. Schaefer,<sup>10</sup> Benjamin R. Setterholm,<sup>3</sup> David Wilner,<sup>7</sup> Zhaohuan Zhu<sup>14</sup>

\*Correspondence to: s.kraus@exeter.ac.uk

**Affiliations:** <sup>1</sup>Univ. of Exeter, School of Physics & Astronomy, Stocker Road, Exeter, EX4 4QL, UK, <sup>2</sup>School of Physics and Astronomy, Univ. of Leicester, University Road, Leicester, LE1 7RH, UK, <sup>3</sup>Univ. of Michigan, 311 West Hall, 1085 South Univ. Ave. Ann Arbor, MI 48109, USA, <sup>4</sup>Instituut voor Sterrenkunde, KU Leuven, Celestijnenlaan 200D, 3001 Leuven, Belgium, <sup>5</sup>Georgia State University, P.O. Box 5060, Atlanta, GA 30302, USA, <sup>6</sup>Univ. of North Carolina Greensboro, Greensboro, NC 27402, USA, <sup>7</sup>Harvard Smithsonian Center for Astrophysics, 60 Garden Street, Cambridge, MA 02138, USA, <sup>8</sup>Steward Observatory, University of Arizona, 993 N. Cherry Ave, Tucson, AZ 85721, USA, <sup>9</sup>Carnegie Institution for Science, 5241 Broad Branch Road, NW, Washington, DC 20015, USA, <sup>10</sup>The CHARA Array of Georgia State University, Mount Wilson, CA 91023, USA, <sup>11</sup>Instituto de Física y Astronomía, Universidad de Valparaíso, Casilla 5030, Valparaíso, Chile, <sup>12</sup>Boston Univ. 725 Commonwealth Avenue, Boston, MA

02215, USA, <sup>13</sup>Université Grenoble Alpes, CNRS, IPAG, 38000 Grenoble, France, <sup>14</sup>Univ. of Nevada, 4505 S. Maryland Parkway, Las Vegas, NV 89154, USA

**Abstract:**

**In young multiple stellar systems the gravitational influence of the stars shapes the circumstellar disk, controlling accretion and the material available for planet formation. Our observations of the triple system GW Orionis provide direct evidence for disk tearing, where the gravitational torques due to misaligned disk/orbit planes warp the disk and break the inner disk into precessing rings. We image an eccentric ring that is misaligned with respect to the orbital planes and outer disk, and casts shadows on the strongly warped intermediate disk. Our ring/warp geometry constraints and the fully characterized perturber orbits make the system a potential Rosetta Stone for studying disk hydrodynamics. The ring might offer suitable conditions for planet formation, providing a mechanism for forming wide-separation planets on highly oblique orbits.**

**Main text:**

Stars form through fragmentation & collapse of molecular clouds, where the most frequent outcome is a gravitationally bound multiple, such as a binary or triple system (1, 2). As the system evolves, the stars continue to interact dynamically with each other and with the circum-multiple disk that facilitates the accretion onto the stars. Recent numerical simulations (3, 4) proposed a novel hydrodynamic effect, disk tearing, that might sculpt the disks around multiple systems where the orbital plane is significantly misaligned with respect to the disk plane. The gravitational torque from the misaligned companions can break the

disk apart into several distinct planes. The resulting rings separate from the disk plane and precess around the central objects (5).

Previous work identified misalignments in disks, but it has not been possible to link the misaligned structures clearly to disk tearing, either due to the non-detection of the perturber (e.g. (6)) or a poor characterization of its orbit (e.g. (7, 8, 9)). Here, we report the detection of an eccentric, strongly misaligned disk ring orbiting the GW Orionis triple system and determine its 3-dimensional structure and spatial orientation. At the same time we tightly constrain the orbits of the stars, allowing us to link the properties of the observed disk to disk tearing based on first-principle simulations.

GW Orionis is located at a distance of  $388\pm 5$  parsec in the  $\lambda$  Orionis star forming region (10) and has an age of  $1.0\pm 0.1$  million years (11). The hierarchical system consists of a close (1.2 astronomical unit, au) binary with a  $\sim 242$  days period on a nearly-circular orbit (A-B system; 12, 13) and a tertiary that orbits in  $\sim 11$  years at  $\sim 8$  au separation (AB-C system; 14, 15). We have monitored the orbital motion of the system over 11 years using near-infrared interferometry (1.4-2.4  $\mu\text{m}$  thermal continuum emission; Fig. S9), which results in tight constraints on the mass of the three stars ( $M_A=2.47\pm 0.33$ ,  $M_B=1.43\pm 0.18$ , and  $M_C=1.36\pm 0.28$  solar masses) and the orientation of the orbits. The orbits of the inner pair (A-B) and the tertiary (AB-C) are misaligned by  $13.9\pm 1.1^\circ$  with respect to each other.

In parallel to characterizing the stellar orbits, we use high-angular resolution thermal dust imaging (obtained with sub-millimeter and near-infrared interferometry) and scattered light imaging of dust shadows (obtained with visible and near-infrared adaptive-optics imaging polarimetry) to constrain the dust distribution in the system. Combining both of these

techniques enables us to constrain the 3-dimensional orientations of the disk components and to detect the warped intermediate disk region.

The cold dust (traced by 1.3mm continuum emission) is arranged in three rings, where the two outermost rings (with radii of  $334\pm 13$  and  $182\pm 12$  au; labeled R1 and R2 in Fig. 1A) are centered on the A+B binary and seen at an inclination of  $142\pm 1^\circ$  and  $143\pm 1^\circ$  respectively, corresponding to retrograde rotation with the Eastern side tilted towards us by  $38^\circ/37^\circ$ . The third, innermost ring R3 has a projected radius of  $43.5\pm 1.1$  au and appears in projection more circular than R1/R2 and offset with respect to the center-of-mass of the system (Fig. 1B). We also see dust emission between R2 and R3 as well as inside or R3, with a factor  $\sim 10$  lower flux density than in the neighboring rings. Inside of the tertiary orbit we detect a circumbinary ring (R4) with radius  $2^{+2.5}_{-0.8}$  au around the A-B binary (Fig. 1F), based on near-infrared interferometry modeling (16).

Our infrared polarimetric images show asymmetric scattered light emission extending from  $\sim 50$  to  $\sim 500$  au. The emission is arranged in four arcs (A1 to A4 in Figs. 1C and 1D) with the Eastern side appearing brighter than the Western side, which is consistent with forward-scattering from a disk where the Eastern side faces towards the observer. The dimmer regions separating the arcs A1, A2, and A3 coincide with the dust rings R1, R2, and R3 (Fig. 1E), which we interpret as a shadowing effect (16). Arcs A3 and A4 appear to be part of an elliptical structure, whose semi-major axis orientation (along position angle,  $PA\sim 60^\circ$ , measured East of North) clearly deviates from the orientation of the outer disk (along  $PA\sim 0^\circ$ ). Furthermore, we see two sharp shadows extending in radial direction (S1, S2), where the Eastern shadow S1 shows a distinct change in direction at  $\sim 100$  au separation (Fig. 1D), exhibiting a North-South orientation at radii  $< 100$  au ( $PA\sim 0^\circ$ , labeled  $S1_{\text{inner}}$ ) and South-East orientation at larger radii ( $PA\sim 135^\circ$ , labeled  $S1_{\text{outer}}$ ). Besides these sharply defined shadows, we detect two

broader shadows extending in North-East (S3) and South-West direction (S4). Furthermore, a filamentary scattered-light structure ( $F_{\text{scat}}$ ) extends from the inner-most arc (A3) towards the stars (Fig. 1D).

The outer rings R1 and R2 are well-aligned with respect to each other, but strongly misaligned with respect to the orbital plane of the stars, confirming a tentative finding based on the disk gas kinematics by Czekala et al. (15). Several physical mechanisms have been proposed that might have resulted in this primordial misalignment, including turbulent disk fragmentation (17), perturbation by other members in a stellar cluster (18), star-disk capture (19), or the infall of material whose angular momentum vector was misaligned to that of the gas that formed the stars initially (20, 21).

The innermost ring R3 is strongly misaligned both with respect to the outer disk and to the orbits, likely due to the dynamical interaction with the inner multiple system. We built a 3-dimensional model that aims to reproduce both the on-sky projected shape of the dust rings as well as the shadows seen in scattered light. Inspired by hydrodynamics simulations (e.g. (4, 22)) and the detection of lower-density dust between R2 and R3 in our sub-millimeter image, we model this region as a warped dust filament that extends smoothly from ring R2 to an break radius, where the warp is truncated. Our modeling efforts (16) indicate that we see material at this inner truncation orbit directly in our scattered light images, namely as the apparent ellipse formed by the scattered light arcs A3 and A4. The part of the warp facing away from Earth is located South-East and fully illuminated by the stars, appearing therefore as the prominent scattered light arc A3 (Figs. 1C and 2C). The opposite side of the warp, located North-West of the stars, is facing towards us, allowing us to see only the outer surface that is not illuminated by the stars, resulting in the much weaker scattered light arc A4.

Extinction due to dust in the warp reduces the illumination on the North-Western side of the disk and causes the broad shadows S3 and S4 that we see towards  $PA \sim 240^\circ$  and  $\sim 20^\circ$ , corresponding to the directions with the highest radial column density in the warp. The surface of the warp also acts as screen for shadows cast by the geometrically thin misaligned ring R3, resulting in the sharply-defined shadow S1. The curvature that we see in S1 can then be understood as a projection effect, where  $S1_{\text{inner}}$  is the shadow cast on the warped surface inside of R2, while  $S1_{\text{outer}}$  is the shadow on the non-warped outer disk (Fig. 2A). Reproducing the on-sky projected shape of R3, its off-center position with respect to the stars, as well the shape of shadows S1 and S2 requires us to adopt a significant non-zero eccentricity for ring R3 ( $e=0.3 \pm 0.1$ ), with the stars located in one of the focal points of the ellipse. The 3-dimensional orientation of the orbits and of the detected dust rings is illustrated in Fig. 2 and parameterized in Tables S5+S6.

Facchini et al. (5) predicted the observational signatures of broken protoplanetary disks, both in sub-millimeter thermal emission and near-infrared scattered light. They considered a circumbinary disk misaligned by  $60^\circ$  with the binary orbit, similar to the misalignment angles observed for GW Orionis ( $51.1 \pm 1.1^\circ$  for the A-B orbit and  $38.5 \pm 0.8^\circ$  for the (AB)-C orbit). We see remarkable similarities between our observations and their synthetic images, including a misaligned ring in sub-millimeter emission and a strong azimuthal asymmetry in scattered light with sharply-defined shadows.

Also, the detected eccentricity of ring R3 matches the prediction that the Kozai-Lidov mechanism should induce oscillations in the orbital inclination and eccentricity for broken rings (4, 22, 23). We compare the radius of R3 (43 au) to analytic estimates of the tearing radius, defined as the point in a circumbinary disk where the external torque exerted by a

misaligned binary exceeds the internal torque due to pressure forces (4). We find that the predicted tearing radius matches the size of R3 for realistic disk viscosity values ( $\alpha < 0.05$ ), suggesting that this disk region is susceptible to disk tearing (16).

Our tight observational constraints on the orbital parameters of the GW Orionis system allow us to simulate the response of the disk to the specific triple star orbits using dedicated smoothed particle hydrodynamic (SPH) and radiative transfer simulations. We parameterize the initial disk with the observed total dust mass (24) and adopt the actually measured stellar orbits and outer disk orientation (for details on the simulation setup see (16)). After letting the simulation evolve for a few thousand years, we see that the gravitational torque from the misaligned triple system breaks the disk apart into several distinct planes and forms an eccentric ring with radius  $\sim 40$  au that precesses around the inner multiple system with a precession period of  $\sim 8,000$  years (snapshot in Fig. 3). The size of the ring in the simulation, its eccentricity, asymmetric azimuthal density profile (with highest density near apsis), and strong misalignment with respect to the outer disk qualitatively matches the characteristics of the ring R3 observed at sub-millimeter wavelengths. The agreement between our hydrodynamic simulation and observation strongly suggests that ring R3 in the GW Orionis system is due to disk tearing. The SPH simulation also develops a low-density warp (Fig. 3D), whose properties and spatial orientation broadly resemble the disk warp in our scattered light model (Fig. 2). While it is out of the scope of this study to reproduce the observed structures quantitatively with SPH modeling we note that GW Orionis is at present the only pre-main-sequence multiple system with fully characterized orbits and well-constrained misaligned disk features, providing a unique benchmark for studying disk tearing and to constrain fundamental hydrodynamic parameters, such as the disk viscosity.

Our study shows that disk tearing does occur in young multiple systems and that it is a viable mechanism to produce disk warps and misaligned disk rings that can precess around the inner system. Extinction from this out-of-plane dust, as well as phased accretion onto the circumtertiary disk ( $D_c$ ) near apoastron/periastron, might also be responsible for some of the photometric variability and the quasi-periodic eclipse events observed towards GW Orionis, as supported by observations presented in the supplementary text. Furthermore, by transporting material out of the disk plane, the observed disk tearing effect provides a new mechanism for forming planets on oblique or retrograde orbits. About 40% of short-period exoplanets ( $\lesssim 40$  days orbital period) orbit their star on oblique or even retrograde orbits (25), where planet-planet scattering and tidal interactions from wider-orbiting planets are the preferred explanation (26). For long-period planets and circumbinary planets only few measurements exist, with all cases indicating good alignment between the stellar spin and planet orbit plane (the most inclined known circumbinary planet is Kepler-413b, where an obliquity of  $2.5^\circ$  has been measured (27)). Our study provides the strongest evidence yet that disk tearing can induce extreme primordial misalignments in a planet-forming disk. We find that the broken ring R3 contains 18 Earth masses in dust (16), which could suffice for planet formation to occur. This implies that there may exist a significant, yet undiscovered population of long-period planets on highly oblique orbits that has formed from rings around misaligned multiple systems.

## References and Notes

- (1) R.D. Mathieu, Pre-main-sequence binary stars. *Annu. Rev. Astron. Astrophys.* **32**, 465-530 (1994) doi: 10.1146/annurev.aa.32.090194.002341

- (2) G. Duchene, A. Kraus, Stellar Multiplicity. *Ann. Rev. Astron. Astrophys.* **51**, 269-310 (2013)  
doi: 10.1146/annurev-astro-081710-102602
- (3) C. Nixon, A. King, D. Price, J. Frank, Tearing up the disk: How black holes accrete. *Astrophys. J. Lett.* **757**, L24 (2012) doi: 10.1088/2041-8205/757/2/L24
- (4) C. Nixon, A. King, D. Price, Tearing up the disc: misaligned accretion on to a binary. *Mon. Not. R. Astron. Soc.* **434**, 1946-1954 (2013) doi: 10.1093/mnras/stt1136
- (5) S. Facchini, A. Juhász, G. Lodato, Signatures of broken protoplanetary discs in scattered light and in sub-millimetre observations. *Mon. Not. R. Astron. Soc.* **473**, 4459-64475 (2018)  
doi: 10.1093/mnras/stx2523
- (6) P. Pinilla, M. Benisty, J. de Boer, C.F. Manara, J. Bouvier, C. Dominik, C. Ginski, R.A. Loomis, A. Sicilia Aguilar, Variable outer disk shadowing around the dipper star RXJ1604.3-2130. *Astrophys. J.* **868**, 85-99 (2018) doi: 10.3847/1538-4357/aae824
- (7) S. Casassus, S. Marino, S. Pérez, P. Roman, A. Dunhill, P. J. Armitage, J. Cuadra, A. Wootten, G. van der Plas, L. Cieza, V. Moral, V. Christiaens, M. Montesinos, Accretion kinematics through the warped transition disk in HD142527 from resolved CO(6-5) observations. *Astrophys. J.* **811**, 1-14 (2015) doi:10.1088/0004-637X/811/2/92
- (8) S. Marino, S. Perez, S. Casassus, Shadows cast by a warp in the HD142527 protoplanetary disk. *Astrophys. J. Lett.* **798**, L44, 1-4 (2015) doi:10.1088/2041-8205/798/2/L44
- (9) G. M. Kennedy, L. Matrà, S. Facchini, J. Milli, O. Panić, D. Price, D. J. Wilner, M. C. Wyatt, B. M. Yelverton, A circumbinary protoplanetary disk in a polar configuration. *Nature Astron.* **3**, 230-235 (2019) doi: 10.1038/s41550-018-0667-x

- (10) M. Kounkel, L. Hartmann, M. Mateo, J. I. Bailey III, Kinematics of the optically visible YSOs towards the Orion B Molecular Cloud. *Astrophys. J.* **844**, 138, 1-8 (2019) doi: 10.3847/1538-4357/aa7dea
- (11) N. Calvet, J. Muzerolle, C. Briceño, J. Hernández, L. Hartmann, J. L. Saucedo, K. D. Gordon, The Mass Accretion Rates of Intermediate-Mass T Tauri Stars. *Astron. J.* **128**, 1294-1318 (2004) doi: 10.1086/422733
- (12) R. D. Mathieu, F. C. Adams, D. W. Latham, The T Tauri Spectroscopic Binary GW Orionis. *Astron. J.* **101**, 2184, (1991) doi: 10.1086/115841
- (13) L. Prato, D. Ruíz-Rodríguez, L.H. Wassermann, Orbital solution for the spectroscopic binary in the GW Ori hierarchical triple. *Astrophys. J.* **852**, 38-42 (2018) doi: 10.3847/1538-4357/aa98df
- (14) J.-P. Berger, J. D. Monnier, R. Millan-Gabet, S. Renard, E. Pedretti, W. Traub, C. Bechet, M. Benisty, N. Carleton, P. Huguenaier, P. Kern, P. Labeye, F. Longa, M. Lacasse, F. Malbet, K. Perraut, S. Ragland, P. Schloerb, P. A. Schuller, E. Thiebaut, First astronomical unit scale image of the GW Orionis triple system. Direct detection of a new stellar companion. *Astron. Astrophys. Lett.* **529**, L1, 1-4 (2011) doi: 10.1051/0004-6361/201016219
- (15) I. Czekala, S. M. Andrews, G. Torres, J. E. Rodriguez, E. L. N, Jensen, K. G. Stassun, D. W. Latham, D. J. Wilner, M. A. Gully-Santiago, K. N. Grankin, M. B. Lund, R. B. Kuhn, D. J. Stevens, R. J. Siverd, D. James, B. S. Gaudi, B. J. Shappee, T. W.-S. Holoien, The Architecture of the GW Ori Young Triple-star System and Its Disk: Dynamical Masses, Mutual Inclinations, and Recurrent Eclipses. *Astrophys. J.* **851**, 132-161 (2017) doi: 10.3847/1538-4357/aa9be7
- (16) Additional data, materials, and methods are provided as supplementary materials

- (17) S. S. R. Offner, K. M. Kratter, C. D. Matzner, M. R. Krumholz, R. I. Klein, The formation of low-mass binary star systems via turbulent fragmentation. *Astrophys. J.* **725**, 1485-1494 (2010) doi: 10.1088/0004-637X/725/2/1485
- (18) C. J. Clarke, J. E. Pringle, Accretion disc response to a stellar fly-by. *Mon. Not. R. Astron. Soc.* **261**, 190-202 (1993) doi: 10.1093/mnras/261.1.90
- (19) C. J. Clarke, J. E. Pringle, The role of discs in the formation of binary and multiple star systems. *Mon. Not. R. Astron. Soc.* **249**, 588-598 (1991) doi: 10.1093/mnras/249.4.588
- (20) M. R. Bate, G. Lodato, J. E. Pringle, Chaotic star formation and the alignment of stellar rotation with disc and planetary orbital axes. *Mon. Not. R. Astron. Soc.* **401**, 1505-1513 (2010) doi: 10.1111/j.1365-2966.2009.15773.x
- (21) M. R. Bate, On the diversity and statistical properties of protostellar discs. *Mon. Not. R. Astron. Soc.* **475**, 5618-5658 (2018) doi: 10.1093/mnras/sty169
- (22) S. Doğan, C. Nixon, A. King, D. J. Price, Tearing up a misaligned accretion disc with a binary companion. *Mon. Not. R. Astron. Soc.* **449**, 1251-1258 (2015) doi: 10.1093/mnras/stv347
- (23) R. G. Martin, C. Nixon, S. H. Lubow, P. J. Armitage, D. J. Price, S. Doğan, A. King, The Kozai-Lidov mechanism in hydrodynamical disks. *Astrophys. Lett. J.* **792**, L33 (2014) doi: 10.1088/2041-8205/792/L33
- (24) M. Fang, A. Sicilia-Aguilar, V. Roccatagliata, D. Fedele, T. Henning, C. Eiroa, A. Müller, GW Orionis: Inner disk readjustments in a triple system. *Astron. Astrophys.* **570**, A118, 1-22 (2014) doi: 10.1051/0004-6361/201424146

- (25) D. Lai , F. Foucart, D. N. C. Lai, Evolution of spin direction of accreting magnetic protostars and spin-orbit misalignment in exoplanetary systems. *Mon. Not. R. Astron. Soc.* **412**, 2790-2798 (2011) doi: 10.1111/j.1365-2966.2010.18127.x
- (26) S. Albrecht, J. N. Winn, J. A. Johnson, A.W. Howard, G. W. Marcy, R. P. Butler, P. Arriagada, J. D. Crane, S. A. Shectman, I. B. Thompson, T. Hirano, G. Bakos, J. D. Hartman. Obliquities of Hot Jupiter Host Stars: Evidence for Tidal Interactions and Primordial Misalignments. *Astrophys. J.* **757**, 1-25 (2012) doi: 10.1088/0004-637X/757/1/18
- (27) V. B. Kostov, P. R. McCullough, J. A. Carter, M. Deleuil, R. F. Diaz, D. C. Fabrycky, G. Hébrard, T. C. Hinse, T. Mazeh, J. A. Orosz, Z. I. Tsvetanov, W. F. Welsh, Kepler-413b: A slightly misaligned, Neptune-size Transiting Circumbinary Planet. *Astrophys. J.* **784**, 14-32 (2014) doi: 10.1088/0004-637X/784/1/14
- (28) R. G. Petrov, et al., *Astron. Astrophys.* **464**, 1 (2007)
- (29) E. Tatulli, et al., *Astron. Astrophys.* **464**, 29 (2007)
- (30) A. Chelli, O. H. Utrera, G. Duvert, *Astron. Astrophys.* **502**, 705 (2009)
- (31) S. Kraus, et al., *Astron. Astrophys.* **497**, 195 (2009)
- (32) A. Mérand, P. Bordé, V. Coudé Du Foresto, *Astron. Astrophys.* **447**, 783 (2006)
- (33) M. F. Skrutskie, et al., *Astron. J.* **131**, 1163 (2006)
- (34) R. M. Cutri, et al., WISE All-Sky Data Release, VizieR Online Data Catalog 2311, <http://cdsads.u-strasbg.fr/abs/2012yCat.2311....0C>, accessed 2019 December 10 (2012)
- (35) M. Kounkel, et al., *The Astrophysical Journal* **834**, 142 (2017)
- (36) M. Fang, et al., *Astron. Astrophys.* **603**, A132 (2017)
- (37) Gravity Collaboration, et al., *Astron. Astrophys.* **602**, A94 (2017)

- (38) V. Lapeyrere, *et al.*, *SPIE Conf. Ser.* (2014), vol. **9146** of *Society of Photo-Optical Instrumentation Engineers (SPIE) Conference Series*, p. 91462D
- (39) S. Kraus, *et al.*, *SPIE Conf. Ser.* (2018), vol. **10701** of *Society of Photo-Optical Instrumentation Engineers (SPIE) Conference Series*, p. 1070123
- (40) N. Anugu, *et al.*, *SPIE Conf. Ser.* (2018), vol. **10701** of *Society of Photo-Optical Instrumentation Engineers (SPIE) Conference Series*, p. 1070124
- (41) J. D. Monnier, J.-P. Berger, R. Millan-Gabet, T. A. ten Brummelaar, *SPIE Conf. Ser.*, W. A. Traub, ed. (2004), vol. **5491** of *Society of Photo-Optical Instrumentation Engineers (SPIE) Conference Series*, p. 1370
- (42) J. D. Monnier, *et al.*, *SPIE Conf. Ser.* (2010), vol. **7734** of *Society of Photo-Optical Instrumentation Engineers (SPIE) Conference Series*, p. 77340G
- (43) D. J. Wilner, W. J. Welch, *Astrophys. J.* **427**, 898 (1994)
- (44) R. D. Mathieu, *et al.*, *Astron. J.* **109**, 2655 (1995)
- (45) M. J. Ireland, A. L. Kraus, *Astrophys. J. Lett.* **678**, L59 (2008)
- (46) S. Kraus, *et al.*, *Astrophys. J.* **768**, 80 (2013)
- (47) M. Willson, *et al.*, *Astron. Astrophys.* **595**, A9 (2016)
- (48) B. Macintosh, *et al.*, *Proceedings of the National Academy of Science* **111**, 12661 (2014)
- (49) J. D. Monnier, *et al.*, *Astrophys. J.* **838**, 20 (2017)
- (50) A. Laws, T. J. Harries, B. R. Setterholm, *Astrophys. J.* in press; arXiv e-prints p. arXiv:1911.04214 (2019)
- (51) J. L. Beuzit, *et al.*, *arXiv e-prints* p. arXiv:1902.04080 (2019)
- (52) K. Dohlen, *et al.*, *Ground-based and Airborne Instrumentation for Astronomy II* (2008), vol. **7014** of *SPIE Conf. Ser.*, p. 70143L
- (53) H. M. Schmid, *et al.*, *Astron. Astrophys.* **619**, A9 (2018)

- (54) H. Avenhaus, *et al.*, *Astrophys. J.* **863**, 44 (2018)
- (55) J. Kluska, *et al.*, *Astrophys. J.* **855**, 44 (2018)
- (56) M. E. van den Ancker, *High Resolution Infrared Spectroscopy in Astronomy*, H. U. Käufl, R. Siebenmorgen, A. F. M. Moorwood, eds. **309** (2005)
- (57) D. F. M. Folha, J. P. Emerson, *Astron. Astrophys.* **365**, 90 (2001)
- (58) S. Kraus, *et al.*, *Astrophys. J.* **752**, 11 (2012)
- (59) K.-H. Hofmann, G. Weigelt, *Astron. Astrophys.* **278**, 328 (1993)
- (60) S. Kraus, *et al.*, *Nature* **466**, 339 (2010)
- (61) S. Kraus, *et al.*, *Astrophys. J. Lett.* **746**, L2 (2012)
- (62) C. Pinte, F. Ménard, J.P. Berger, M. Benisty, F. Malbet, *Astrophys. J. Lett.* **673**, L63 (2008)
- (63) S. Kraus, *et al.*, *Astron. Astrophys.* **508**, 787 (2009)
- (64) A. Tokovinin, ORBIT3—Orbits of Triple Stars; *Zenodo* **51824** (2017)  
doi:10.5281/zenodo.51824
- (65) A. Tokovinin, D. W. Latham, *Astrophys. J.* **838**, 54 (2017)
- (66) J. Fekel, F. C., *Astrophys. J.* **246**, 879 (1981)
- (67) A. N. Cox, *Allen's astrophysical quantities*, 4<sup>th</sup> ed. Publisher: New York: AIP Press; Springer 2000. Arthur N. Cox, ed. (2000)
- (68) S. Kraus, *et al.*, *Astron. Astrophys.* **466**, 649 (2007)
- (69) R. Storn, K. Price, *Journal of Global Optimization* **11**, 341 (1997)
- (70) A. Isella, C. J. Chandler, J. M. Carpenter, L. M. Pérez, L. Ricci, *Astrophys. J.* **788**, 129 (2014)
- (71) J. E. Pineda, *et al.*, *Astrophys. J.* **871**, 48 (2019)

- (72) N. I. Shakura, R. A. Sunyaev, *Astron. Astrophys.* **24**, 337 (1973)
- (73) R. Teague, J. Bae, E. A. Bergin, T. Birnstiel, D. Foreman-Mackey, *Astrophys. J. Lett.* **860**, L12 (2018)
- (74) N. Calvet, *et al.*, *Astron. J.* **128**, 1294 (2004)
- (75) A. P. Whitworth, *et al.*, *Mon. Not. R. Astron. Soc.* **277**, 727 (1995)
- (76) M. R. Bate, I. A. Bonnell, *Mon. Not. R. Astron. Soc.* **285**, 33 (1997)
- (77) W. Benz, *Numerical Modelling of Nonlinear Stellar Pulsations Problems and Prospects*, J. R. Buchler, ed. (1990), p. 269
- (78) M. R. Bate, I. A. Bonnell, N. M. Price, *Mon. Not. R. Astron. Soc.* **277**, 362 (1995)
- (79) D. J. Price, M. R. Bate, *Mon. Not. R. Astron. Soc.* **377**, 77 (2007)
- (80) B. A. Ayliffe, M. R. Bate, *Mon. Not. R. Astron. Soc.* **408**, 876 (2010)
- (81) T. J. Harries, T. J. Haworth, D. Acreman, A. Ali, T. Douglas, *Astronomy and Computing* **27**, 63 (2019)
- (82) B. T. Draine, H. M. Lee, *Astrophys. J.* **285**, 89 (1984)
- (83) E. Tognelli, P. G. Prada Moroni, S. Degl'Innocenti, *Astron. Astrophys.* **533**, A109 (2011)
- (84) W. K. M. Rice, P. J. Armitage, K. Wood, G. Lodato, *Mon. Not. R. Astron. Soc.* **373**, 1619 (2006)
- (85) R. R. Rafikov, *Astrophys. J.* **837**, 163 (2017)
- (86) V. S. Shevchenko, K. N. Grankin, M. A. Ibragimov, S. Y. Melnikov, *Information Bulletin on Variable Stars* **3746**, 1 (1992)
- (87) V. S. Shevchenko, K. N. Grankin, S. Y. Mel'Nikov, S. A. Lamzin, *Astronomy Letters* **24**, 528 (1998)
- (88) M. R. Bate, *et al.*, *Mon. Not. R. Astron. Soc.* **317**, 773 (2000)

(89) J. L. Smallwood, S. H. Lubow, A. Franchini, R. G. Martin, *Mon. Not. R. Astron. Soc.* **486**, 2919 (2019)

(90) P. Artymowicz, S. H. Lubow, *Astrophys. J. Lett.* **467**, L77 (1996)

**Acknowledgements:** This paper is based on observations made with ESO telescopes at the La Silla Paranal Observatory. We thank the ESO Paranal Staff for support for conducting the observations. This paper makes use of ALMA data set ADS/JAO.ALMA #2018.1.00813.S. ALMA is a partnership of ESO (representing its member states), NSF (USA) and NINS (Japan), together with NRC (Canada), MOST and ASIAA (Taiwan), and KASI (Republic of Korea), in cooperation with the Republic of Chile. The Joint ALMA Observatory is operated by ESO, AUI/NRAO and NAOJ. The Joint ALMA Observatory is operated by ESO, AUI/NRAO and NAOJ. This work is based in parts upon observations obtained with the Georgia State University Center for High Angular Resolution Astronomy Array at Mount Wilson Observatory. The CHARA Array is supported by the National Science Foundation under Grant No. AST-1636624 and AST-1715788. Institutional support has been provided from the GSU College of Arts and Sciences and the GSU Office of the Vice President for Research and Economic Development. This paper is based in parts on observations obtained at the Gemini Observatory, which is operated by the Association of Universities for Research in Astronomy, Inc., under a cooperative agreement with the NSF on behalf of the Gemini partnership: the NSF (United States), the National Research Council (Canada), CONICYT (Chile), Ministerio de Ciencia, Tecnologia e Innovacion Productiva (Argentina), and Ministerio da Ciencia, Tecnologia e Inovacao (Brazil). Some of the data presented herein were obtained at the W. M. Keck Observatory from telescope time allocated to the National Aeronautics and Space Administration through the agency's scientific partnership with the California Institute of Technology and the University of California. The Observatory was made possible by the generous financial support of the W. M. Keck Foundation. The authors wish to recognize and acknowledge the very significant cultural role and reverence that the summit of Mauna Kea has always had within the indigenous Hawaiian community. We are most fortunate to have

the opportunity to conduct observations from this mountain. Some of the figures were produced using SPLASH (Price 2007), an SPH visualization tool publicly available at <http://users.monash.edu.au/~dprice/splash>.

**Funding:** Our team acknowledges support from the European Research Council under the European Commission's Horizon 2020 program (Grant Agreement Numbers 639889 and 681601) and Seventh Framework program (Grant Agreement Number 339248). A.L. wishes to thank the Science Technology and Facilities Council (STFC) for the studentship that supported this work (project reference 1918673). J.D.M. and E.A.R. acknowledge funding from National Science Foundation grant NSF-AST1506540 and NASA grant NNX16AD43G. JK acknowledges support from the research council of the KU Leuven under grant number C14/17/082. The SPH and radiative transfer calculations discussed in this paper were performed on the University of Exeter Supercomputer, Isca.

**Author contributions:** S.K. conceived the project, initiated the ALMA, VLT, VLTI, and CHARA observing programs, modeled the infrared and sub-millimeter data, fitted the triple star orbit, and wrote the initial manuscript. A.K. worked on implementing the scattered light model and the ALMA data reduction. A.K.Y. and M.R.B. set up and ran the radiative transfer and SPH simulations. J.D.M. initiated the GPI observing program. H.A. processed the IRDIS data set. J.K. processed the ZIMPOL data set. A.S.E.L. and E.A.R. processed the GPI data set. M.W. and M.J.I. processed the NIRC2 data set. S.K., J.D.M., N.A., C.L.D., J.E., T.G., A.L., C.L., J.-B.L. G.H.S., and B.R.S. contributed to building and commissioning the MIRC-X instrument. S.K., J.D.M., T.J.H., A.N.A., F.C.A., S.M.A., J.B., N.C., C.E., L.H., S.H., D.W., and Z.Z. contributed to the GPI survey. All co-authors provided input on the manuscript.

**Competing interests:** There are no conflicts of interest.

**Data availability:** The VLT and VLTI data reported in this paper are archived in the ESO Science Archive (<http://archive.eso.org>) under program IDs 082.C-0893(A), 384.D-0482(A, B), 084.C-0848(A, B, C, D, E, F, G), 086.C-0684(A, B), 088.C-0868(A), 090.C-0070(A), 094.C-0721(A), 098.C-0910(A), 100.C-0686(A,B,C), and 102.C-0778(A). The ALMA data is archived in the ALMA Science Archive (<http://almascience.nrao.edu/aq/>) under project code ADS/JAO.ALMA#2018.1.00813.S. The MIRC-X data will be made available at the Open Research Exeter repository (<https://ore.exeter.ac.uk>). GPI data are accessible from the Gemini Observatory archive (<https://archive.gemini.edu>).

**List of Supplementary materials:**

Materials and Methods

Supplementary Text

Tables S1 – S6

Figs. S1 – S19 (S18 is an interactive 3-D graphics that could potentially also be moved to the main text, in case the journal allows embedded 3-D graphics for online publication)

References (28 – 90)

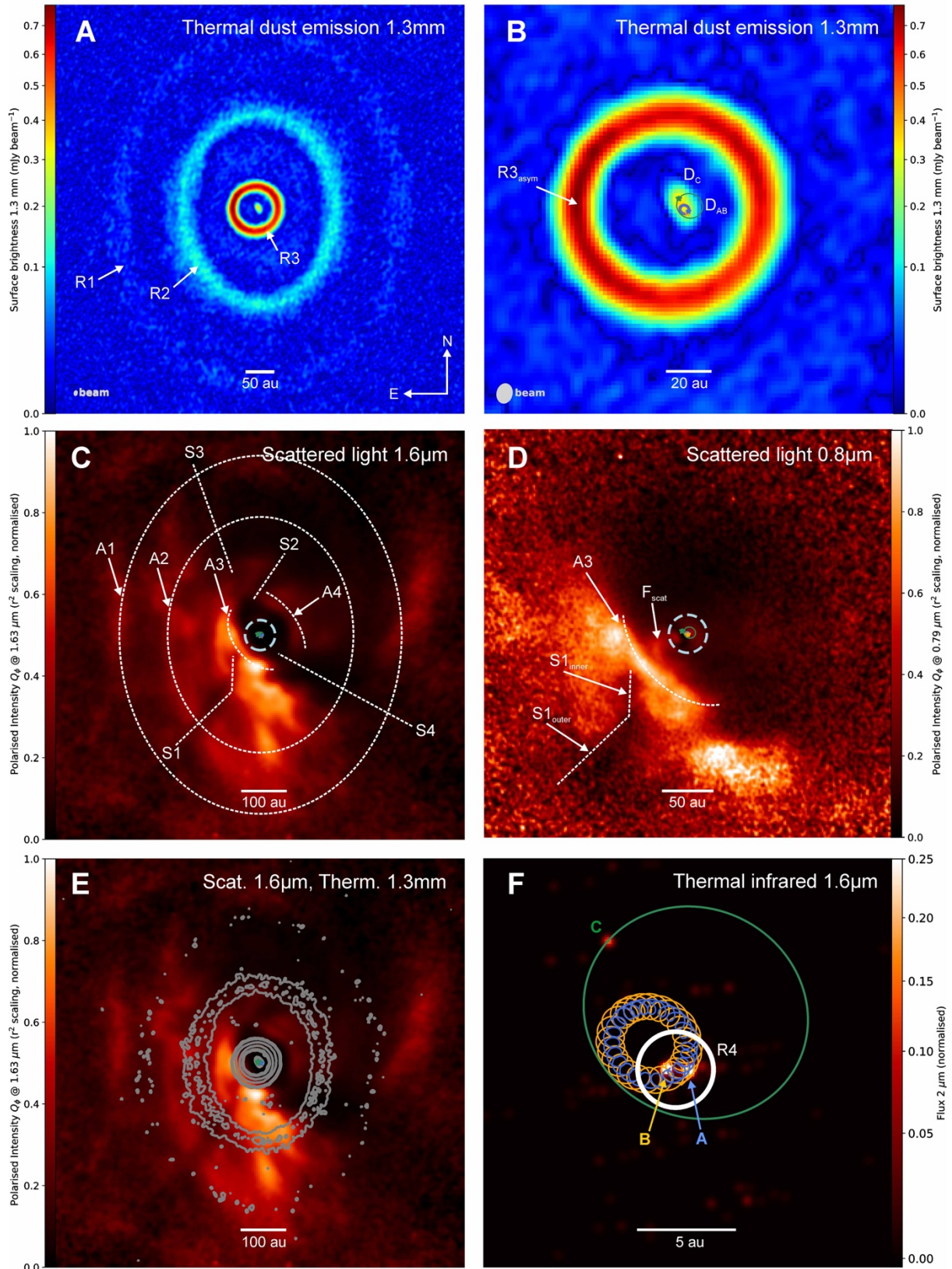


Fig. 1: High-angular resolution imaging of the disk components around GW Orionis, in 1.3 mm thermal dust continuum emission (A,B), near-infrared and visible-wavelength scattered light

(C,D,E), and 1.6  $\mu\text{m}$  infrared emission (F). The scattered-light images show polarised intensity in local Stokes vector  $Q\phi$  and we indicate the inner working angle of the observations (dashed blue circles). The main components seen in the images are labelled, including three rings (R1,R2,R3), an asymmetry in the ring R3 ( $R3_{\text{asym}}$ ), and dust emission close to the stars ( $D_{\text{AB}}, D_{\text{C}}$ ). In the scattered-light images, we detect four arc structures (A1,A2,A3,A4) and a filamentary structure ( $F_{\text{scat}}$ ). We see four shadows in radial direction (S1,S2,S3,S4), where S1 clearly follows a different position angle at projected separations  $<100$  au ( $S1_{\text{inner}}$ ) than further out ( $S1_{\text{outer}}$ ). In panel (E) the 1.3 mm image is over-plotted as contours on the 1.6  $\mu\text{m}$  scattered light image (contours at 0.035/0.1/0.15 mJy beam $^{-1}$ ). Panel (F) shows our 1.6  $\mu\text{m}$  aperture synthesis image from 2019 August 27 with the location of the circumbinary disk (R4) indicated as white circle. The emission from R4 is not visible in the image, but has been deduced from visibility data modeling (16). In panels (B)-(F) the orbits and position of the stars at the time of observation is indicated (green/orange/blue curves and symbols).

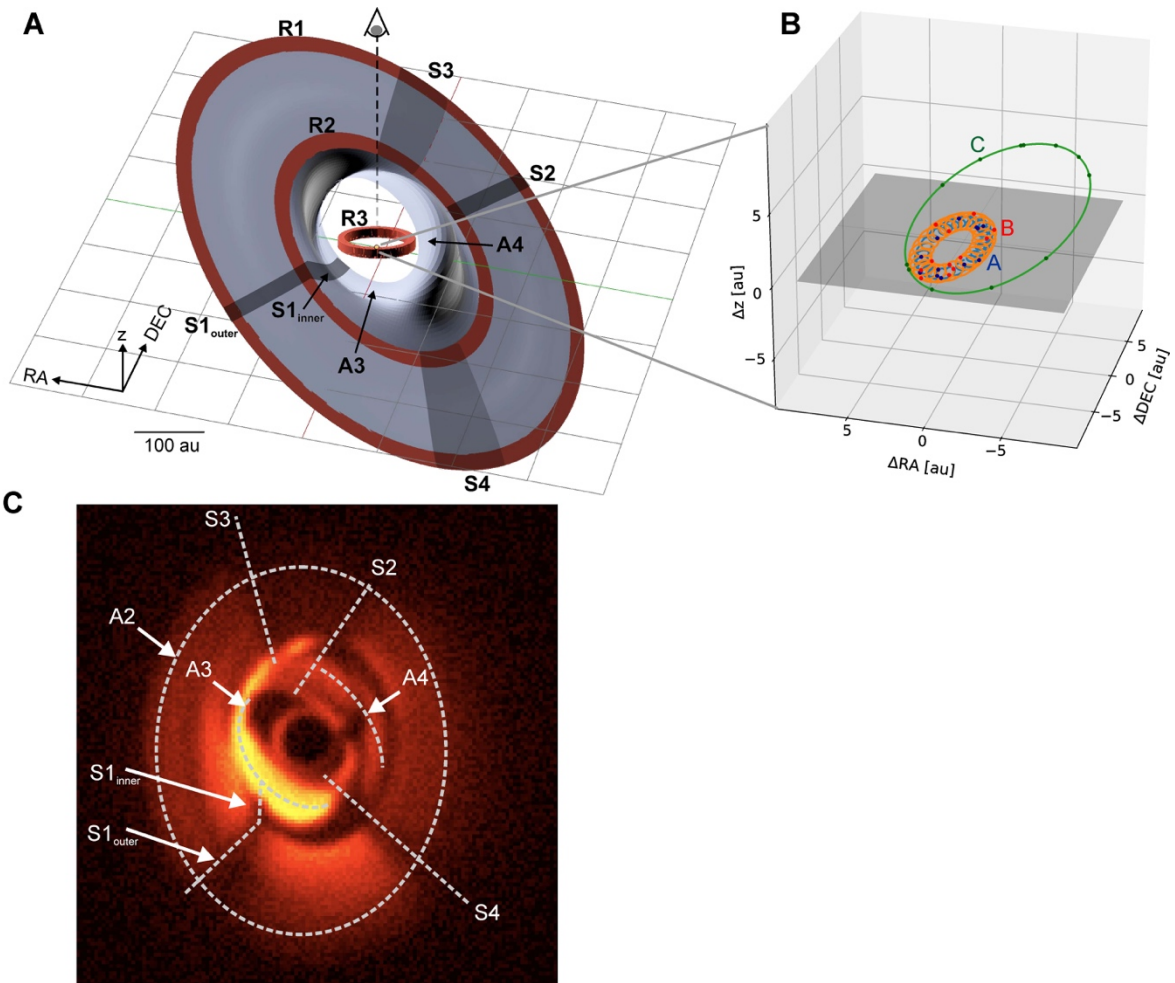


Fig. 2: Scattered light model (16) to constrain the eccentricity and 3-dimensional orientation of ring R3 and the geometry of the disk warp based on the morphology of the shadows seen in scattered light. (A): Illustration of the 3-dimensional orientation of the disk components in the model. (B): Orientation of the orbits in the hierarchical triple system, with the stellar positions at the time of our astrometry measurements indicated (blue/orange/green curves and points). The coordinate system is centered on the center-of-mass of the system. The grey planes represents the sky (RA-DEC) plane, while the z-axis points towards the observer. (C) Synthetic image computed from our scattered light model, convolved to match the resolution achieved in the observation, and with the position of the scattered light features from Figs. 1C+1D indicated.

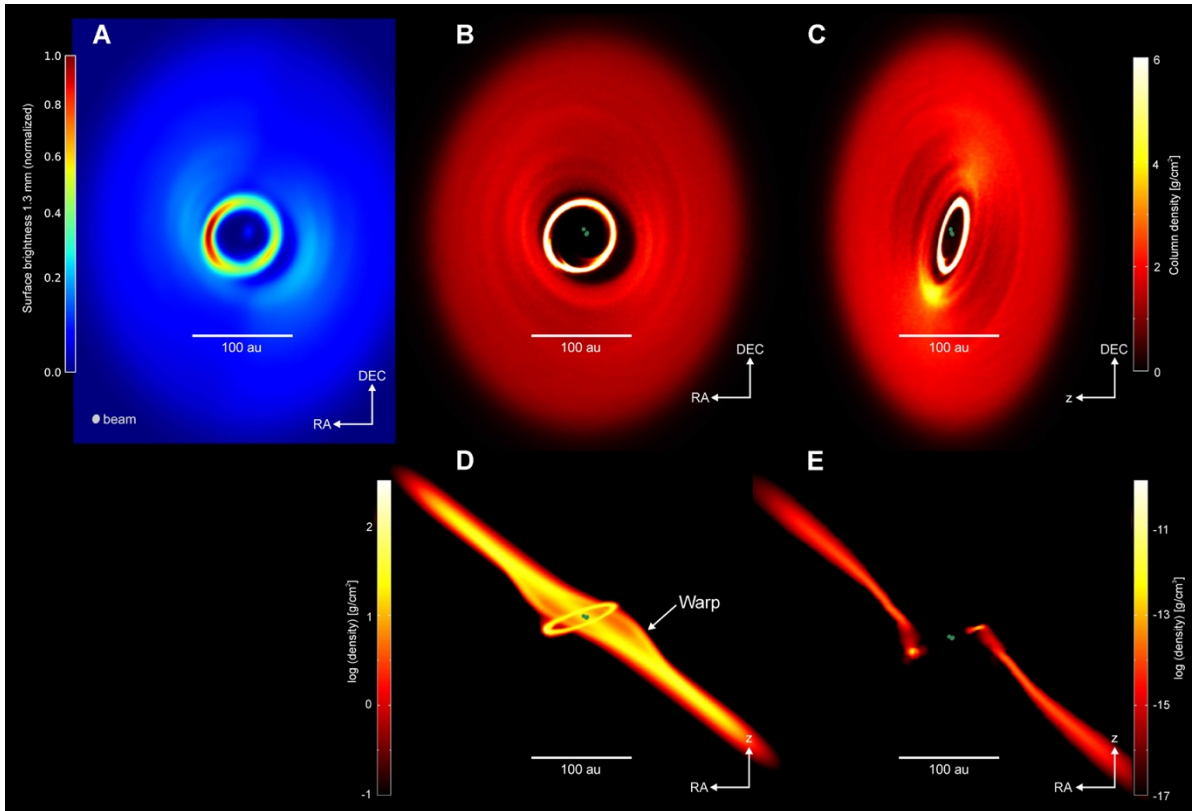


Fig. 3: Smoothed particle hydrodynamic simulation based on the measured GW Orionis orbits and system parameters, after letting the system evolve for 9500 years. (A): radiative transfer model image computed for the wavelength of our sub-millimeter observation and convolved with the interferometric beam. (B): column density projected on the sky plane, with North up and East left. (C),(D): column density projected in the z-DEC plane and RA-z plane (with positive z facing towards the observer). (E): density cut along the RA-z plane.

# Disk tearing in a young triple star system with misaligned disk/orbit planes

Stefan Kraus,<sup>1\*</sup> Alexander Kreplin,<sup>1</sup> Alison K. Young,<sup>1,2</sup> Matthew R. Bate,<sup>1</sup>  
John D. Monnier,<sup>3</sup> Tim J. Harries,<sup>1</sup> Henning Avenhaus, Jacques Kluska,<sup>1,4</sup>  
Anna S. E. Laws,<sup>1</sup> Evan A. Rich,<sup>3</sup> Matthew Willson,<sup>1,5</sup>  
Alicia N. Aarnio,<sup>6</sup> Fred C. Adams,<sup>3</sup> Sean M. Andrews,<sup>7</sup>  
Narsireddy Anugu,<sup>1,3,8</sup> Jaehan Bae,<sup>3,9</sup> Theo ten Brummelaar,<sup>10</sup> Nuria Calvet,<sup>3</sup>  
Michel Curé,<sup>11</sup> Claire L. Davies,<sup>1</sup> Jacob Ennis,<sup>3</sup>  
Catherine Espaillat,<sup>3,12</sup> Tyler Gardner,<sup>3</sup> Lee Hartmann,<sup>3</sup>  
Sasha Hinkley,<sup>1</sup> Aaron Labdon,<sup>1</sup> Cyprien Lanthermann,<sup>13</sup>  
Jean-Baptiste LeBouquin,<sup>3,13</sup> Gail H. Schaefer,<sup>10</sup> Benjamin R. Setterholm,<sup>3</sup>  
David Wilner,<sup>7</sup> Zhaohuan Zhu,<sup>14</sup>

<sup>1</sup>Univ. of Exeter, School of Physics & Astronomy, Stocker Road, Exeter, EX4 4QL, UK,

<sup>2</sup>School of Physics and Astronomy, Univ. of Leicester, University Road, Leicester, LE1 7RH, UK,

<sup>3</sup>Univ. of Michigan, 311 West Hall, 1085 South Univ. Ave. Ann Arbor, MI 48109, USA,

<sup>4</sup>Instituut voor Sterrenkunde, KU Leuven, Celestijnenlaan 200D, 3001 Leuven, Belgium,

<sup>5</sup>Georgia State University, P.O. Box 5060, Atlanta, GA 30302, USA,

<sup>6</sup>Univ. of North Carolina Greensboro, Greensboro, NC 27402, USA,

<sup>7</sup>Harvard Smithsonian Center for Astrophysics, 60 Garden Street, Cambridge, MA 02138, USA,

<sup>8</sup>Steward Observatory, University of Arizona, 993 N. Cherry Ave, Tucson, AZ, 85721, USA,

<sup>9</sup>Carnegie Institution for Science, 5241 Broad Branch Road, NW, Washington, DC 20015, USA,

<sup>10</sup>The CHARA Array of Georgia State University, Mount Wilson, CA 91023, USA,

<sup>11</sup>Instituto de Fisica y Astronomia, Universidad de Valparaiso, Casilla 5030, Valparaiso, Chile

<sup>12</sup>Boston Univ. 725 Commonwealth Avenue, Boston, MA 02215, USA,

<sup>13</sup>Université Grenoble Alpes, CNRS, IPAG, 38000 Grenoble, France,

<sup>14</sup>Univ. of Nevada, 4505 S. Maryland Parkway, Las Vegas, NV 89154, USA

\*To whom correspondence should be addressed; E-mail: s.kraus@exeter.ac.uk

**In this document, we provide detailed information on our methods and additional material (Sect. S1), including on the observational setup of our infrared and sub-millimeter observations (Sect. S1.1), our data modeling procedure (Sect. S1.2), and our smoothed particle hydrodynamic (SPH) simulations (Sect. S1.3). We provide supplementary text (Sect. S2) to support our argument that the observed misaligned ring is caused by disk tearing (Sect. S2.1) and that dust in the inner disk (Sect. S2.2) and phased accretion onto the circumtertiary disk (Sect. S2.3) might be responsible for the photometric variability and the quasi-periodic eclipse events observed towards GW Orionis.**

## **S1 Materials and Methods**

### **S1.1 Observations**

The data used for this study is summarized in Table S1. In the following sections, we provide further details on the instrument setup that was used for our observations and the data reduction process. All infrared interferometric observations on GW Ori (using the AMBER, GRAVITY, and MIRC-X instruments) were interleaved with observations on calibrator stars of known uniform disk diameter  $d_{\text{UD}}$ . The properties of these calibrators are listed in Table S2.

#### **S1.1.1 VLTI/AMBER near-infrared interferometry**

We observed GW Ori with the AMBER instrument (28) and ESO’s Very Large Telescope Interferometer (VLTI). The observations were conducted at seven epochs in the period between 2008 December 15 and 2015 January 1 (Table S1) and used the VLTI 8.2 m unit telescopes, resulting in projected baseline lengths between 24.4 and 129.9 m. The data covers wavelengths between 1.4 and 2.5  $\mu\text{m}$  (H- and K-band) with spectral resolution  $R = \lambda/\Delta\lambda = 35$ .

We extract wavelength-dependent visibilities and closure phases from the data using the

Table S1. Observation log of our observations

Instrument	Spectral setting	Date (UT)	Time (UT)	DIT [s]	NEXP	Telescope(s) configuration	Calibrators
AMBER	LR-HK	2008-12-15	04:30	0.050	5	UT1-UT3-UT4	HD 29150, HD 30912
AMBER	LR-HK	2009-12-05	05:21	0.050	10	UT1-UT2-UT4	HD 34203
AMBER	LR-HK	2009-12-06	06:43	0.021	10	UT1-UT3-UT4	HD 34203
AMBER	LR-HK	2009-12-06	07:49	0.021	8	UT1-UT3-UT4	HD 34203
AMBER	LR-HK	2009-12-06	08:51	0.021	8	UT1-UT3-UT4	HD 34203
AMBER	LR-HK	2009-12-31	02:20	0.021	12	UT1-UT2-UT4	HD 37128
AMBER	LR-HK	2009-12-31	03:05	0.021	6	UT1-UT2-UT4	HD 37128
AMBER	LR-HK	2010-01-01	03:50	0.021	10	UT1-UT3-UT4	HD 34203
AMBER	LR-HK	2010-01-01	04:24	0.021	6	UT1-UT3-UT4	HD 34203
AMBER	LR-HK	2010-01-01	07:12	0.021	12	UT2-UT3-UT4	HD 42807
AMBER	LR-HK	2010-12-17	02:55	0.050	10	UT2-UT3-UT4	HD 34203
AMBER	LR-HK	2010-12-17	03:41	0.050	15	UT2-UT3-UT4	HD 41794
AMBER	LR-HK	2010-12-18	07:10	0.027	5	UT2-UT3-UT4	HD 34203
AMBER	LR-HK	2011-12-09	04:02	0.026	10	UT1-UT3-UT4	HD 34203
AMBER	LR-HK	2011-12-09	05:27	0.026	10	UT1-UT3-UT4	HD 34203
AMBER	LR-HK	2012-10-29	05:20	0.026	6	UT1-UT2-UT4	HD 22781
AMBER	LR-HK	2012-10-29	06:38	0.026	10	UT1-UT2-UT4	HD 34203
AMBER	LR-HK	2012-10-29	09:15	0.026	5	UT1-UT2-UT4	HD 28462
AMBER	LR-HK	2015-01-01	02:17	0.026	5	UT1-UT3-UT4	HD 37128
MIRC-X	LR-H	2019-08-27	12:06	0.0028	5	S1-S2-E1-E2-W1-W2	HD 240579
GRAVITY	MR	2017-10-25	06:14	30	6	A0-B2-C1-D0	HD 244179, HD 38117
GRAVITY	MR	2017-10-25	07:43	30	6	A0-B2-C1-D0	HD 244179, HD 37926
GRAVITY	MR	2018-02-06	01:30	30	4	A0-G1-J2-J3	HD 38117
NIRC2/SAM	L-band	2013-11-16	14:26	1	$3 \times 20$	Keck2	hd 36045, hd 38899
GPI	J-coron-pol	2018-01-04	02:33	29	$2 \times 35$	Gemini-S	–
GPI	H-coron-pol	2018-01-04	03:59	29	$2 \times 35$	Gemini-S	–
SPHERE/ZIMPOL	I'-band, SlowPol	2018-10-15	06:58	8	$6 \times 4$	UT3	–
SPHERE/IRDIS	H-band, SlowPol	2018-11-16	06:07	16	$9 \times 6$	UT3	–
ALMA	continuum 1.3 mm	2019-07-05	13:47	2782		C43-9/10	J0530+1331, J0510+1800
CRIFES	Long-slit spectros.	2012-11-11	06:09	120	$2 \times 3 \times 6$	UT1	Hip 25662

amdlib software, release 3 (29, 30). In order to minimize the effect of residual telescope jitter, we follow the standard AMBER data reduction procedure and select the interferograms with the 10% best signal-to-noise ratio. In addition, we reject scans where the optical-path-delay exceeded  $4 \mu\text{m}$  in order to improve the visibility calibration. The wavelength calibration was done using the telluric absorption bands between the J/H and H/K-band (see Appendix A in (31)).

Table S2. Information on interferometric calibrators

Star	$H$	$K$	$N$	Spectral Type	$d_{\text{UD}}$ [mas]
HD 22781	6.69	6.61	–	K0	$0.228 \pm 0.016^{\text{a}}$
HD 28462	7.21	7.14	–	K1	$0.179 \pm 0.004^{\text{a}}$
HD 29150	6.08	5.99	–	G5	$0.285 \pm 0.020^{\text{a}}$
HD 30912	5.07	4.98	–	F2IV	$0.407 \pm 0.028^{\text{a}}$
HD 34203	5.47	5.46	–	A0V	$0.228 \pm 0.016^{\text{a}}$
HD 37128	2.41	2.27	–	B0Iab	$0.670 \pm 0.040^{\text{a}}$
HD 37926	5.60	5.44	–	K0	$0.393 \pm 0.009^{\text{a}}$
HD 38117	5.12	4.91	–	K0	$0.494 \pm 0.016^{\text{a}}$
HD 41794	6.19	6.13	–	A5	$0.213 \pm 0.015^{\text{a}}$
HD 42807	5.01	4.85	–	G2V	$0.486 \pm 0.034^{\text{a}}$
HD 240579	6.37	6.15	–	K0	$0.293 \pm 0.007^{\text{a}}$
HD 244179	6.02	5.87	–	K0	$0.327 \pm 0.008^{\text{a}}$
HD 39400	–	–	1.83	K1.5IIb	$2.387 \pm 0.138^{\text{b}}$
HD 37160	–	–	1.40	K0IIIb	$2.079 \pm 0.204^{\text{b}}$

<sup>a</sup>UD diameter taken from (32).

<sup>b</sup>UD diameter taken from CalVin.

Note. — The H and K-band magnitudes were taken from the 2MASS point source catalog (33) and the N-band magnitudes from the WISE all-sky survey (34).

Table S3. Adopted system parameters

	Symbol	Unit	Value	Reference
Distance <sup>a</sup>	$d$	[pc]	$388 \pm 5$	(35)
Effective temperature	$T_{\text{eff}}$	[K]	5500	(36)
Bolometric luminosity	$L_{\text{sun}}$	$[L_{\text{sun}}]$	$48 \pm 10$	(24)
Extinction	$A_V$	[mag]	$1.5 \pm 0.1$	(24)
Disk total mass (gas+dust)	$M_{\text{disk}}$	$[M_{\text{sun}}]$	0.12	(36)

<sup>a</sup>We follow earlier studies (e.g. (15)) and adopt the distance estimate from (35). Their distance estimate reports smaller measurement uncertainties than other studies and is compatible with the GAIA DR2 value of  $398 \pm 10$  pc, without being potentially systematically biased by astrometric motion induced by the triple system.

### **S1.1.2 VLT/GRAVITY near-infrared interferometry**

On three nights in 2017 and 2018 we acquired observations with the VLT/GRAVITY instrument (37). The observations combined the light from the four VLT 1.8 m auxiliary telescopes and covered the K-band (1.9...2.5  $\mu\text{m}$ ) with  $R = 500$ . For the 2017 observations, the telescopes were in the compact configuration (A0-B2-D0-C1), corresponding to projected baselines in the 8.4 to 31.4 m range. The 2018 observation was conducted with the extended configuration (A0-G1-J2-J3), resulting in projected baseline lengths between 57.5 and 129.4 m. Wavelength-differential visibilities and phases were extracted using the GRAVITY pipeline (Release 1.2.4, (38)).

### **S1.1.3 CHARA/MIRC-X near-infrared interferometry**

In 2019 we acquired another epoch of near-infrared interferometry (1.45...1.8  $\mu\text{m}$ ; H-band) using the recently-commissioned MIRC-X instrument (39, 40). Building on the MIRC combiner (41, 42) that was in operation between 2005 and 2017, this instrument combines all six telescopes of the CHARA array simultaneously, resulting in visibility measurements on 15 baselines and 20 closure phase measurements in a single pointing. Our data probes projected baseline length between 32.0 and 330.7 m, which increased the angular resolution and astrometric accuracy by factor 2.5 compared our earlier VLT observations, while using the significantly smaller CHARA 1 m apertures (compared to the 8.2 m apertures that were used with AMBER, and 1.8 m apertures used with GRAVITY). The data was recorded using the PRISM50 spectral mode, which covers the 1.5-1.72  $\mu\text{m}$  range (H-band) with spectral resolution  $R = 50$ .

For the data reduction, we used the MIRC-X data reduction pipeline<sup>1</sup>.

---

<sup>1</sup>The MIRC-X pipeline is available at [https://gitlab.chara.gsu.edu/lebouquj/mircx\\_pipeline.git](https://gitlab.chara.gsu.edu/lebouquj/mircx_pipeline.git).

#### S1.1.4 ALMA sub-millimeter interferometry

Our ALMA band 6 data was recorded on 2019 July 5 as part of ALMA Cycle 6 program 2018.1.00813.S. The array included 44 antennas that were arranged in configuration C43-9/10, covering baseline lengths between  $L_{\min} = 241.0$  m and  $L_{\max} = 10,240.9$  m. The observations cycled between GW Ori and the phase calibrator J0530+1331. In total, 46.4 min data were recorded on-source of GW Ori. The bright quasar J0510+1800 was used as bandpass and flux calibrator, while J0539+1433 was observed as check source. Our setup included four spectral basebands centered on 230.55, 232.5, 217.5, and 219.465 GHz. Each spectral band covers a bandwidth of 1875 MHz with a spectral resolution of 1.129 MHz. Here, we focus on interpreting the continuum geometry of the disk around GW Ori and leave the interpretation of the spectral line data to a future study.

The standard flagging and calibration was done using CASA version 5.6.0. Self-calibration was performed with the shortest phase and amplitude cycle of 10 and 60 seconds, respectively. For the image reconstruction process we used only line-free spectral channels and employed the Clean algorithm with a Briggs weight of 0.5, which resulted in a beam size of  $24 \times 19$  mas (along PA  $-13^\circ$ ) and a root-mean-square noise of  $60 \mu\text{Jy beam}^{-1}$ .

Given the use of the extended array configuration C43-9/10 our observations lack sensitive to extended emission. The maximum recoverable scale is  $0.6\lambda/L_{\min} \approx 0.67''$  (43)<sup>2</sup>, which indicates that our image captures all emission within ring R3 and on smaller scales. The flux in the extended ring R1 (and possibly R2 and Rwrap) is likely underestimated, which is consistent with the fact that the total flux density in our image (0.089 Jy) is about a factor 3 lower than flux measurements derived with other facilities at significantly lower resolution (e.g.  $0.255 \pm 0.060$  Jy from (44)). Therefore, as part of our modeling efforts (Sect. S1.2.5) we report only lower

---

<sup>2</sup>see also ALMA technical handbook: <https://almascience.eso.org/documents-and-tools/cycle6/alma-technical-handbook>

limits on the sub-millimeter fluxes and the derived mass estimates for the most extended spatial components. This spatial filtering affects the brightness, but not the location nor the geometry of the extended rings in the image. Accordingly, our data set provides reliable inclination and position angle estimates for our physical interpretation and modeling.

### **S1.1.5 Keck2/NIRC2 L-band aperture masking interferometry**

We recorded L-band aperture masking interferometry with the NIRC2 instrument mounted on the Keck2 10 m telescope. We used a detector integration time of 1 s and recorded 3 calibrator-science cycles on GW Ori ( $3 \times 20$  frames) with the the calibrators hd 36045 ( $1 \times 20$  frames) and hd 38899 ( $2 \times 20$  frames) interleaved. In order to derive calibrated visibilities and closure phases, we follow the data reduction procedure outlined in (45–47).

### **S1.1.6 GPI near-infrared polarimetric imaging**

Imaging polarimetric observations were conducted with the Gemini Planet Imager (GPI; (48)) on 2018 January 4 using both the “J-coron-pol” (J-band;  $\lambda_C = 1235$  nm;  $\Delta\lambda=230$  nm) and “H-coron-pol” (H-band;  $\lambda_C = 1650$  nm;  $\Delta\lambda=300$  nm) instrument setup. We utilized the standard GPI coronagraphic masks that feature a diameter of  $0''.184$  (for J-band) and  $0''.246$  (H-band), respectively.

The data was reduced using the GPI Data Reduction Pipeline (DRP) version 1.5 (ref c0cad3f). We follow the procedure outlined in (49, 50) to derive the local Stokes parameters  $Q_\phi$  and  $U_\phi$ . This representation of the Stokes vector has the advantage that it yields positive  $Q_\phi$  values when the field polarization angle is perpendicular to the vector connecting the pixel and the star’s location. We do not attempt to minimize  $U_\phi$ , as this observable might contain real signal, in particular for disks seen under high inclination. However, for most cases of single-scattering and moderate inclination angles,  $U_\phi$  is expected to remain free of astrophysical signals. Fig. S1 shows the Stokes  $Q_\phi$  and  $U_\phi$  images. For our interpretation we focus on the  $Q_\phi$  maps, as these

maps provide a good measure for the azimuthally polarized flux from the disk.

### **S1.1.7 SPHERE visible + near-infrared polarimetric imaging**

Our polarimetric imaging with the SPHERE instrument (51) utilized both the near-infrared arm (IRDIS, (52)) and the visible-light arm (ZIMPOL, (53)). The IRDIS observations were conducted with the H-band filter (BB\_H,  $\lambda_C = 1625$  nm;  $\Delta\lambda=290$  nm) and the smallest available coronagraphic mask (N\_ALC\_YJ\_S; inner working angle 0.08"). Images for nine polarimetric cycles were recorded, each with six images of 16 s integration time. The ZIMPOL observations were conducted with exceptional seeing conditions (0.3-0.4" FWHM) and using the I'-band filter (I\_PRIM,  $\lambda_C = 789.7$  nm;  $\Delta\lambda=152.7$  nm). We did not use a coronagraphic mask in order to achieve a smaller inner working angle, but required a neutral density filter to avoid saturation (ND\_2.0 filter). Six polarimetric cycle sequences were recorded, each recording 4 images of 8 s integration time for each cycle step.

For the data processing of the IRDIS data, we follow the procedure outlined in (54) and derive Stokes  $Q_\phi$  and  $U_\phi$  maps. To extract the polarized intensity images from ZIMPOL data, we applied the procedure outlined in (55), deriving again  $Q_\phi$  and  $U_\phi$ . The resulting images are shown in Fig. S2.

### **S1.1.8 CRIRES spectro-astrometry**

The near-infrared Br $\gamma$ -line is considered a good accretion tracer (e.g. (56)) and has also been detected towards GW Ori (57). We obtained spectro-astrometric observations with the CRIRES instrument, which allows us to localize the spatial origin of the line emission, and, therefore the sites of ongoing accretion in the GW Ori system.

Our setup was optimized for the spectro-astrometry technique, where we measure the centroid position along the slit direction with high precision in order to derive the photocenter offset in the line with respect to the continuum.

Table S4. Fitting results obtained for our near-infrared interferometric data.

Epoch	$F_B/F_A$	$\rho_{AB}$ [mas]	$\theta_{AB}$ [ $^\circ$ ]	$F_C/F_A$	$\rho_{AC}$ [mas]	$\theta_{AC}$ [ $^\circ$ ]	$F_{\text{ext}}/F_{\text{tot}}$	$\chi_{\text{red}}^2$
2003.913	$0.88 \pm 0.19$	$2.5 \pm 0.2$	$22.4 \pm 6$	$0.22 \pm 0.03$	$23.5 \pm 0.7$	$250 \pm 2$	$0.16^a$	0.3
2004.957	$1.10 \pm 0.25$	$2.8 \pm 0.8$	$151 \pm 3$	$0.36 \pm 0.06$	$18.4 \pm 0.2$	$206 \pm 1$	$0.16^a$	2.1
2005.890	$0.65 \pm 0.44$	$2.6 \pm 0.6$	$11 \pm 2$	$0.31 \pm 0.17$	$13.3 \pm 1.1$	$148 \pm 6$	$0.16^a$	0.2
2008.956	$0.66 \pm 0.06$	$2.66 \pm 0.11$	$147.5 \pm 0.9$	$0.19 \pm 0.02$	$23.12 \pm 0.18$	$10.3 \pm 0.5$	$0.16^a$	0.7
2009.927	$0.97 \pm 0.16$	$2.46 \pm 0.06$	$347.1 \pm 0.5$	$0.21 \pm 0.02$	$25.16 \pm 0.21$	$345.7 \pm 0.1$	$0.16 \pm 0.02$	0.5
2009.995	$0.74 \pm 0.02$	$2.80 \pm 0.02$	$299.4 \pm 0.3$	$0.20 \pm 0.02$	$27.22 \pm 0.08$	$340.7 \pm 0.1$	$0.16^a$	0.2
2010.960	$1.08 \pm 0.10$	$2.38 \pm 0.04$	$120.7 \pm 1.3$	$0.23 \pm 0.01$	$27.00 \pm 0.25$	$328.0 \pm 0.3$	$0.16^a$	1.1
2011.937	$0.71 \pm 0.12$	$2.70 \pm 0.08$	$327.7 \pm 0.6$	$0.26 \pm 0.03$	$30.53 \pm 0.19$	$308.0 \pm 0.2$	$0.16^a$	0.9
2012.825	$1.12 \pm 0.03$	$2.50 \pm 0.02$	$209.2 \pm 0.6$	$0.32 \pm 0.01$	$29.3 \pm 0.1$	$289.1 \pm 0.2$	$0.16^a$	0.9
2015.000	$0.64 \pm 0.03$	$3.18 \pm 0.02$	$93.6 \pm 0.4$	$0.15 \pm 0.01$	$23.8 \pm 0.2$	$249.6 \pm 0.3$	$0.16^a$	0.5
2018.099	$0.83 \pm 0.01$	$2.84 \pm 0.01$	$213.2 \pm 0.2$	$0.47 \pm 0.01$	$9.9 \pm 0.1$	$125.5 \pm 0.1$	$0.16^a$	6.2
2019.652	$0.96 \pm 0.01$	$3.27 \pm 0.01$	$85.2 \pm 0.1$	$0.37 \pm 0.01$	$22.3 \pm 0.01$	$31.9 \pm 0.1$	$0.16^a$	4.8

<sup>a</sup>This parameter was kept fixed in the modeling process.

The CRIRES observations were obtained on 2012 November 11. We recorded spectra for six slit orientations (PA=100, 160, 220 $^\circ$  plus anti-parallel orientations; each with 120 s integrations), which allows us to remove spurious instrumental effects. With a slit width of 0.2'', the spectrum has a resolution is 100,000 and covers the wavelength range from 2.142 to 2.183  $\mu\text{m}$ . Following the science observations, we recorded 28 exposures on the G0V-type standard star Hip 25662 using an integration time of 30 s. We fit the intrinsic Br $\gamma$  absorption in the standard star spectrum and then use the spectrum to correct for telluric absorption in the GW Ori spectrum.

We extract the spectro-astrometric observable (X) and fit the 2-dimensional photocenter offset for each spectral channel, where we correct also for the underlying continuum contributions (Fig. S3). Details of our data processing and analysis procedure can be found in (58).

## S1.2 Modeling

For the stellar parameters of GW Ori, we adopt the values listed in Table S3 throughout our work.

### S1.2.1 Triple star astrometry and circumbinary disk R4

For a first, model-independent inspection of our near-infrared interferometric observations we applied aperture synthesis imaging method to our VLTI and CHARA data. We used our implementation of the Building Block Mapping algorithm (59) that was used already for our earlier studies (31, 60, 61). Representative images for three epochs are shown in Fig. S4.

For each epoch of our VLTI/AMBER+GRAVITY observations, we derive the relative astrometry of the GW Ori system using a triple star model, similar to the one adopted by (14). However, we find that such a 3-point source model provides a poor fit to our VLTI+CHARA data, where we probe up to 10-times higher spatial frequencies than the earlier IOTA observations. Specifically, such a point-source model predicts significantly higher visibilities than measured on long baselines. We are able to improve the fit significantly by introducing an extended emission component. As geometry for this extended emission component, we first considered including an overresolved halo component, as is routinely adopted to reproduce extended flux in T Tauri and Herbig stars (e.g. (62, 63)). Such a model is able to reproduce the VLTI data successfully. However, when we apply this model to the 2003-2005 IOTA data or the short-baseline GRAVITY data, we encounter the problem that the overresolved flux lowers the visibilities too much on short ( $\lesssim 15$  m) baselines, resulting in a very poor fit. This finding provides some constraints on the size of the extended components, as the emission needs to be sufficiently compact to be only marginally resolved on short baselines, but significantly resolved on baselines  $\gtrsim 30$  m. Therefore, the extended emission component is more complex than a Gaussian or uniform intensity profile and we use the combined IOTA+VLTI data to constrain the geometry of this extended emission. We fitted rings with uniform brightness and smoothed rings, where the radial ring intensity profile is parameterized as a Gaussian with fixed FWHM of 0.5 mas in order to avoid unrealistic sharp edges in the brightness profile. We find that a smooth ring centered on the A component provides the best representation of this extended flux

component, with the goodness-of-fit indicator ( $\chi_r^2$ , as defined in ) for different ring radii shown in Fig. S5. This modeling shows the extended near-infrared flux component has a radius of  $\sim 5_{-2}^{+7}$  mas =  $2_{-0.8}^{+2.5}$  au, likely tracing hot dust at the inner edge of a circumbinary disk around the A+B component. Given that our observing setup was optimized for precision astrometry at high spatial frequencies, we lack the  $uv$ -coverage in the short-baseline regime that would be needed to characterize this extended near-infrared emission component further and to determine its precise inclination and orientation in space. However, this might be pursued in future observations.

For the IOTA+VLTI data fits, we represent the stars as point sources. Exploring the long-baseline CHARA/MIRC-X data we find that the visibility level is systematically lower than predicted by the model with point source, resulting in a  $\chi_{\text{ref}}^2 = 5.9$ . The model can be improved by assuming that A+B components are marginally resolved, with  $\chi_{\text{ref}}^2 = 3.6$ , if one adopts uniform disk diameters of  $D_A = 0.6$  mas and  $D_B = 0.57$  mas. This corresponds to 25 and 24 solar diameters, respectively, at the distance of GW Ori, indicating that we resolve some circumstellar dust, possibly arranged in small circumstellar disks. Including resolved emission around the C component does not improve the fit significantly.

In order to illustrate the data quality & quantity obtained with AMBER, GRAVITY, and MIRC-X we show in Figs. S6, S7, and S8 the calibrated visibilities and phases for three representative epochs, overplotted with the best-fit model. The best-fit parameters for all epochs are presented in Table S4. Besides the statistical uncertainties listed in the table, we adopt an additional 5% systematic uncertainty on the derived separation value to account for uncertainties in the spectral calibration of our observations.

### S1.2.2 Astrometric+spectroscopic orbit solution

The existing IOTA+VLTI+CHARA astrometry covers 12 epochs over 15.8 years, or 1.35 ( $\sim 23$ ) full orbital periods of the outer (inner) orbit. The astrometric orbit solution presented by Czekala et al. (15) (C17) was based on data from 3 epochs, covering 17% of the orbit of the outer component, where the astrometry at the third epoch was degenerate due to  $uv$ -coverage limitations, leading to two alternate solutions. Our VLTI+CHARA observations provide astrometry at nine additional epochs, which allows us to resolve these ambiguities and to constrain the 3-dimensional orbits of all stars in the system robustly. Also, the up to 10-times higher angular resolution and denser  $uv$ -coverage of our new near-infrared interferometry allowed us to detect the extended emission component that corresponds to the circumbinary ring R4 (see Sect. S1.2.1) and that affected the earlier-published IOTA astrometry systematically. Specifically, if we re-fit the IOTA data, taking the extended flux into account, we obtain for the inner (A-B) binary system separations that are 21...42% smaller than the Berger et al. (14) separations that were used for the earlier orbit solution. The separations for the outer component are less affected.

The fit was conducted using the 'orbit3' code (64, 65), where we fit the astrometry points (Table S4) simultaneously with the SB2 radial velocity measurements published by (15). We use the radial velocity data that was cleaned by these authors for instrumental effects.

The best-fit orbit solution is presented in Table S5, where  $P$  denotes the orbital period,  $e$  the eccentricity,  $\omega$  the argument of periastron,  $T_0$  the time of periastron passage,  $\gamma$  the velocity of the system center-of-mass,  $i$  the orbital inclination,  $\Omega$  the position angle of the ascending node,  $a$  the orbital semi-major axis, and  $K_A$ ,  $K_B$ ,  $K_C$  the semi-amplitude in radial velocity of the stellar components.  $q$  is the mass ratio  $M_B/M_A$  that is used to compute the 'wobble factor' that describes the motion of the tertiary around the center-of-mass of the A-B system (65).

Both orbits are retrograde, with the ascending node towards the South-West (Fig. S9). Com-

paring the new solution to the orbit solution from (15) (Fig. S10), we find that the short-period orbit is less eccentric (0.069 versus 0.13), while the long-period orbit has significantly higher eccentricity that assumed before (0.379 versus 0.13 for C17 solution #1 or 0.25 for C17 solution #2). Our orbital elements are also consistent with the values for the A-B binary orbit derived by (13), within the relatively large error bars achieved in that study.

We compute the mutual inclination  $\Phi$  between the two orbit planes from their angular momentum vectors following (66):

$$\cos \Phi = \cos i_{A-B} \cos i_{AB-C} + \sin i_{A-B} \sin i_{AB-C} \cos(\Omega_{AB-C} - \Omega_{A-B}) \quad (1)$$

This yields that the A-B and AB-C orbital planes are misaligned by  $\Phi = 13.9 \pm 1.1^\circ$ . The 3-dimensional orientation of the orbits is also illustrated in Figs. S11 (top) and S12 (left), while Fig. S13 shows the on-sky-projected orbits overplotted on VLTI/AMBER and MIRC-X aperture synthesis images.

### S1.2.3 Dynamical masses and orbital parallax

Earlier studies adopted a broad range of mass estimates for GW Ori. For instance, (44) estimated the mass using evolutionary tracks, yielding  $M_A = 2.5 M_\odot$  and  $M_B = 0.5 M_\odot$ , while (14) derived masses of  $M_A = 3.6 M_\odot$  and  $M_B = 3.1 M_\odot$ . However, most of these earlier estimates were based on measurements of the infrared flux ratio between the primary and secondary and our observations show that this flux ratio is highly variable (Table S4 and Fig. S14), likely due to a combination of variable extinction and phase-dependent thermal emission contributions from circumstellar dust (Sect. S2.2). Therefore, we consider the infrared flux ratios as unsuitable to constrain the stellar masses in the system.

The masses of the inner binary (A+B) and the total system (A+B+C) are derived from the measured semi-major axes and periods using Kepler's third law, yielding  $M_{A+B} = 3.90 \pm 0.40 M_\odot$  and  $M_{A+B+C} = 5.26 \pm 0.22 M_\odot$ , respectively. Furthermore, the  $M_A \sin^3 i$  mass

function for A and B are constrained from the measured radial velocity semi-amplitudes, eccentricity, and orbital period. Correcting for the measured inclination yields  $M_A = 2.47 \pm 0.33 M_\odot$  and  $M_B = 1.43 \pm 0.18 M_\odot$ . The radial velocity of the tertiary itself remains undetected – therefore we can only derive a minimum mass for C from the mass function, namely  $M_C > 0.78 \pm 0.10 M_\odot$ . However, based on the total mass constraints, we find that  $M_C = M_{A+B+C} - M_{A+B} = 1.36 \pm 0.28 M_\odot$ . For our error estimation, we include the distance uncertainties as listed in Table S3.

By combining the linear separation from the spectroscopic orbit and the angular separation measured with interferometry, we can derive the orbital parallax of the system and determine the distance to GW Ori. Following (67), we compute the linear scale for the A-B system in astronomical units using

$$a_A = 9.1913 \times 10^5 \frac{P \cdot K_A \cdot \sqrt{1 - e^2}}{\sin(i)} \quad (2)$$

$$a_B = 9.1913 \times 10^5 \frac{P \cdot K_B \cdot \sqrt{1 - e^2}}{\sin(i)}, \quad (3)$$

where the period  $P$  is given in days,  $K_A$  and  $K_B$  are in km/s. The parallax is then  $\pi = a/(a_A + a_B)$ , where  $a$  is the angular semi-major axis in arcseconds. Using the orbital elements from Table S5, this yields a distance of  $387 \pm 27$  pc, which is consistent, both with the distance of  $388 \pm 5$  pc reported by (35) for the Orion Nebula Cluster and  $398 \pm 10$  pc that correspond to the GAIA DR2 parallax for GW Ori.

#### S1.2.4 Asymmetric L-band excess emission near the tertiary

We use our Keck2/NIRC2 aperture masking data in order to search for L-band excess at the position of either of the stars that could be indicative of circumstellar disk emission. The resolution achieved by Keck2 aperture masking does not allow us to resolve the inner binary (A-B). Therefore, we model these observations with a binary model (68), where one component rep-

resents the tertiary (C; with possible contributions from a circumtertiary disk) and the other component the inner binary (A+B system; with possible contributions from component R4). The free parameters are then the separation and position angle between the A-B photocenter and C photocenter, and the L-band flux ratio  $(F_C/F_{A+B})^{3.5\mu\text{m}}$ .

Based on our best-fit orbit solution (Table S5) we predict that the separation (position angle) between the A-B photocenter and component C was  $27.35 \pm 0.3$  mas ( $271.4 \pm 1^\circ$ ) at the time of the NIRC2 observations, where the uncertainties are dominated by the fact that the L-band flux ratio between the A and B component might differ from the H/K band flux ratio as constrained by our infrared long-baseline interferometric observations. If we fit the L-band NIRC2 data with the (AB)-C vector fixed to these values, we find  $(F_C/F_{A+B})^{3.5\mu\text{m}} = 0.30 \pm 0.03$  as best-fit flux ratio, although with a relatively poor  $\chi_r^2 = 24.9$ .

The fit improves significantly if we treat separation and position angle as free fitting parameters, resulting in best-fit values of  $30.7 \pm 0.6$  mas,  $262.7 \pm 1.1^\circ$ , and  $(F_C/F_{A+B})^{3.5\mu\text{m}} = 0.21 \pm 0.02$  ( $\chi_r^2 = 14.0$ ). The measurements are compared to the best-fit model in Fig. S15.

The difference between the measured and predicted separation vector likely indicates that the L-band contains not only photospheric emission, but also circumstellar emission that shifts the photocenter in South-West direction. It is likely that the emission around the inner binary (A-B) contains contributions from the circumbinary disk (R4). However, due to the compactness of this component, it would be difficult to produce the measured photocenter shift only with asymmetries in R4. Therefore, we consider it much more likely that the L-band contains significant contributions from the circumtertiary disk. The tertiary was close to apoastron passage (phase 0.65 in the AB-C orbit) at the time of the NIRC2 observations, and we propose that the excess L-band emission might be associated with hot dust streaming from a circumtriple disk on the circumtertiary disk ( $D_C$ ), causing the measured photocenter shift in North-East direction.

Table S5. Orbital elements

Param.	C17 solution #1		C17 solution #2		This study		
	Orbit $A - B$	Orbit $(AB) - C$	Orbit $A - B$	Orbit $(AB) - C$	Orbit $A - B$	Orbit $(AB) - C$	
$P$	[d]	$241.50 \pm 0.05$	$4246 \pm 66$	$241.49 \pm 0.04$	$4203 \pm 60$	$241.619 \pm 0.05$	$4216.8 \pm 4.6$
$e$		$0.13 \pm 0.01$	$0.13 \pm 0.07$	$0.13 \pm 0.01$	$0.25 \pm 0.08$	$0.069 \pm 0.009$	$0.379 \pm 0.003$
$\omega^a$	[ $^\circ$ ]	$17 \pm 7$	$130 \pm 21$	$16 \pm 6$	$130 \pm 12$	$1 \pm 7$	$105 \pm 1$
$T_0$	JD	$2456682 \pm 4$	$2453911 \pm 260$	$2456681 \pm 4$	$2453878 \pm 130$	$2456674.8 \pm 4.7$	$2453859.6 \pm 4.8$
$\gamma$	[ $\text{km s}^{-1}$ ]	$+28.33 \pm 0.18$	–	$+28.29 \pm 0.19$	–	$+27.96 \pm 0.12$	–
$q$		$0.60 \pm 0.02$	–	$0.60 \pm 0.02$	–	$0.60 \pm 0.02$	–
$i$	[ $^\circ$ ]	$157 \pm 1$	$150 \pm 7$	$157 \pm 1$	$144 \pm 9$	$156 \pm 1$	$149.6 \pm 0.7$
$\Omega^a$	[ $^\circ$ ]	$263 \pm 13$	$282 \pm 9$	$264 \pm 13$	$263 \pm 10$	$258.2 \pm 1.3$	$230.9 \pm 1.1$
$a$	[mas]	$3.2 \pm 0.2$	$23.7 \pm 0.8$	$3.3 \pm 0.2$	$23.6 \pm 0.9$	$3.08 \pm 0.1$	$22.9 \pm 0.1$
$a$	[au]	$1.28 \pm 0.05$	$9.43 \pm 0.33$	$1.31 \pm 0.05$	$9.39 \pm 0.36$	$1.20 \pm 0.04$	$8.89 \pm 0.04$
$K_A$	[ $\text{km s}^{-1}$ ]	$8.34 \pm 0.15$		$8.36 \pm 0.15$		$7.98 \pm 0.16$	
$K_B$	[ $\text{km s}^{-1}$ ]					$13.88 \pm 0.38$	
$K_C$	[ $\text{km s}^{-1}$ ]	$2.38 \pm 0.23$		$2.50 \pm 0.24$		$2.01 \pm 0.20$	
$M_{\text{tot}}$	[ $M_\odot$ ]	$5.7 \pm 0.7$		$6.1 \pm 0.9$		$3.90 \pm 0.40$	
$M_A$	[ $M_\odot$ ]	$2.80^{+0.36}_{-0.31}$		–		$2.47 \pm 0.33$	
$M_B$	[ $M_\odot$ ]	$1.68^{+0.21}_{-0.18}$		–		$1.43 \pm 0.18$	
$M_C$	[ $M_\odot$ ]	$1.15^{+0.40}_{-0.23}$		–		$1.36 \pm 0.28$	

<sup>a</sup>When defining  $\Omega$  and  $\omega$  we follow the convention in the visual binary stars community, where  $\Omega$  gives the longitude of the ascending node (i.e. the node where the motion of the secondary is directed away from the sun) and  $\omega$  is the longitude of the periastron, counted from the ascending node of the secondary.

### S1.2.5 Disk structure: sub-millimeter thermal emission

To enable a quantitative interpretation of the ALMA data, we model the observed brightness distribution using a geometric model. In the model we include the three bright rings labeled R1, R2 and R3 in Fig. 1A. In addition, we include in the model a fourth fainter ring that is located in between R2 and R3, in the following referred to as 'Rwarp'. This fourth ring is not referred to in the main text for simplicity, but it allows us to represent sub-millimeter dust emission that is clearly present near the location of the inferred disk warp (see radial intensity cuts shown in Fig. S16, bottom panels). Therefore, the model includes the following components, where any offsets are measured with respect to the visible-light astrometric position of GW Ori (right ascension  $\alpha = 05^{\text{h}} 29^{\text{m}} 08.3925^{\text{s}}$ ; declination  $\delta = +11^{\text{h}} 52^{\text{m}} 12.654^{\text{s}}$ , J2000):

- (1) three rings ( $i = 1, 2, \text{warp}$ ) with radii  $r_{\text{Ri}}$  and a Gaussian radial intensity profile with half-width-at-half-maximum (HWHM)  $\Theta_{\text{Ri}}$  and flux density  $F_{\nu, \text{Ri}}$  to represent rings R1, R2,

Table S6. Disk model-fitting results for the 1.3 mm ALMA data (Sect. S1.2.5)

Model parameter	Symbol	Unit	Best-fit value
<b>Dust near location of primary/secondary D<sub>AB</sub> (1.3mm)</b>			
Gaussian D <sub>AB</sub> , flux density	$F_{\nu,AB}$	[mJy]	0.12
Gaussian D <sub>AB</sub> , HWHM	$\Theta_{AB}$	[mas]	$\lesssim 4$
Gaussian D <sub>AB</sub> , derived dust mass	$M_{D,AB}$	[ $M_{\text{Earth}}$ ]	0.01
<b>Dust near location of tertiary D<sub>C</sub> (1.3mm)</b>			
Gaussian D <sub>C</sub> , flux density	$F_{\nu,C}$	[mJy]	0.11
Gaussian D <sub>C</sub> , HWHM	$\Theta_C$	[mas]	$\lesssim 4$
Gaussian D <sub>C</sub> , offset dRA	$\Delta\alpha_C$	[mas]	$10.3 \pm 2$
Gaussian D <sub>C</sub> , offset dDEC	$\Delta\delta_C$	[mas]	$-13.0 \pm 2$
Gaussian D <sub>C</sub> , derived dust mass	$M_{D,C}$	[ $M_{\text{Earth}}$ ]	0.009
<b>Ring R1 (1.3mm thermal dust imaging)</b>			
Ring R1, flux density	$F_{\nu,R1}$	[mJy]	$\gtrsim 7.0$
Ring R1, radius	$r_{R1}$	[mas]	$860 \pm 33 (=334 \pm 13 \text{ au})$
Ring R1, inclination	$i_{R1}$	[°]	$142 \pm 1$
Ring R1, HWHM	$\Theta_{R1}$	[mas]	$30 \pm 15$
Ring R1, ascending node <sup>a</sup>	$\Omega_{R1}$	[°]	$180 \pm 8$
Ring R1, derived dust mass	$M_{R1}$	[ $M_{\text{Earth}}$ ]	$\gtrsim 46$
<b>Ring R2 (1.3mm thermal dust imaging)</b>			
Ring R2, flux density	$F_{\nu,R2}$	[mJy]	$\gtrsim 32.0$
Ring R2, radius	$r_{R2}$	[mas]	$470 \pm 32 (=182 \pm 12 \text{ au})$
Ring R2, inclination	$i_{R2}$	[°]	$143 \pm 1$
Ring R2, HWHM	$\Theta_{R2}$	[mas]	$53.4 \pm 18$
Ring R2, ascending node <sup>a</sup>	$\Omega_{R2}$	[°]	$180 \pm 4$
Ring R2, derived dust mass	$M_{R2}$	[ $M_{\text{Earth}}$ ]	$\gtrsim 153$
<b>Ring Rwrap (1.3mm thermal dust imaging)</b>			
Ring Rwrap, flux density	$F_{\nu,Rwrap}$	[mJy]	$\gtrsim 5.2$
Ring Rwrap, radius	$r_{Rwrap}$	[mas]	$270 \pm 12 (=105 \pm 5 \text{ au})$
Ring Rwrap, inclination	$i_{Rwrap}$	[°]	$143 \pm 2$
Ring Rwrap, HWHM	$\Theta_{Rwrap}$	[mas]	$47.3 \pm 4$
Ring Rwrap, ascending node <sup>a</sup>	$\Omega_{Rwrap}$	[°]	$180 \pm 8$
Ring Rwrap, derived dust mass	$M_{Rwrap}$	[ $M_{\text{Earth}}$ ]	$\gtrsim 10.3$
<b>Ring R3 (1.3mm thermal dust imaging)</b>			
Ring R3, flux density	$F_{\nu,R3}$	[mJy]	$23.7 \pm 0.3$
Ring R3, semi-minor axis ( $e = 0$ , fixed) <sup>b</sup>	$b_{R3}$	[mas]	$112 \pm 3 (=43.5 \pm 1.1 \text{ au})$
Ring R3, inclination ( $e = 0$ , fixed) <sup>b</sup>	$i_{R3,e=0}$	[°]	$169.5 + / - 1.0$
Ring R3, HWHM	$\Theta_{R3}$	[mas]	$15.5 \pm 4.6$
Ring R3, offset dRA	$\Delta\alpha_{R3}$	[mas]	$22.98 \pm 0.25$
Ring R3, offset dDEC	$\Delta\delta_{R3}$	[mas]	$-2.35 \pm 0.15$
Ring R3, asymmetry, PA	$\theta_{R3,asym}$	[°]	$47 \pm 9$
Ring R3, asymmetry, amplitude	$a_{R3,asym}$		$0.17 \pm 0.04$
Ring R3, asymmetry, stretch-factor	$\gamma_{R3,asym}$		$0.41 \pm 0.02$
Ring R3, derived dust mass	$M_{R3}$	[ $M_{\text{Earth}}$ ]	17.9
<b>(including 1.6 <math>\mu\text{m}</math>/0.8 <math>\mu\text{m}</math> scattered light imaging constraints)</b>			
Ring R3, inclination ( $e$ free)	$i_{R3}$	[°]	$155 \pm 20$
Ring R3, eccentricity	$e_{R3}$		$0.3 \pm 0.1$
Ring R3, ascending node	$\Omega_{R3}$	[°]	$285 \pm 30$
Ring R3, semi-major axis ( $e$ free) <sup>c</sup>	$a_{R3}$	[mas]	$122 (=47 \text{ au})$

<sup>a</sup>For all rings we identify the southern node as the ascending node, which is consistent with the rings being in retrograde rotation (i.e. following the rotation direction of the stellar orbits) and the Northern part of the rings receding from the observer, as derived from CO rotation measurements ( (36) and (15)).

<sup>b</sup>This inclination estimate assumes that the ring has no intrinsic eccentricity, i.e. that it is intrinsically centro-symmetric. Our scattered light modeling shows that this assumption is not valid for ring R3 – the inclination, argument of periastron, and semi-major axis that corresponds to an intrinsically eccentric ring are reported further below.

<sup>c</sup>This parameter is not fitted, but determined to match the on-sky projected shape of R3 based on the fitted values for  $i_{R3}$ ,  $e_{R3}$ , and  $\Omega_{R3}$ .

Note. — As before, we define inclination 0° as face-on. PAs are measured East of North and along the disk minor axis (coinciding with the disk rotation axis).

and Rwrap. The rings are projected to mimic inclination effects (with inclination angle  $i_{\text{Ri}}$  and the PA of the ascending node  $\Omega_{\text{Ri}}$ ). In order to define the ascending node, we assume that the rings rotate in retrograde motion (i.e. in clockwise direction on the sky), following the same rotation direction as the stellar orbits. We tested whether the fit could be improved by allowing these components to be offset with respect to the origin of the coordinate system – however, we could not observe any significant improvement in the fit and therefore kept the rings centered on the position of the stars.

- (2) another ring, representing ring R3, with the same free parameters as noted above, but an azimuthal modulation that we parameterize as  $f_{\text{R3}}(\theta) = (1 - a_{\text{R3}} \sin(\theta - \theta_{\text{R3asym}}))^{\gamma_{\text{R3asym}}}$ . The ring is allowed an offset with respect to the origin of the coordinate system ( $\Delta\alpha_{\text{R3}}$ ,  $\Delta\delta_{\text{R3}}$ ).
- (3) two Gaussians with HWHM  $\Theta_{\text{AB}}$  ( $\Theta_{\text{C}}$ ) and flux density  $F_{\nu, \text{AB}}$  ( $\Theta_{\text{C}}$ ) to represent the inner components  $\text{D}_{\text{AB}}$  ( $\text{D}_{\text{C}}$ ). The location of the first component is fixed at the origin of the coordinate system, while the offset of the second Gaussian is a free parameters ( $\Delta\alpha_{\text{C}}$ ,  $\Delta\delta_{\text{C}}$ ).

The geometric model is convolved with the interferometric beam and then fitted to the observed image with a Differential Evolution optimisation algorithm (69). The best-fit parameters are reported in Table S6. We note that the values derived for the ring components assumes that the underlying 3-dimensional geometries are rings, which might not be justified for ring R3. Therefore, in Sect. S1.2.6 we also consider that the R3 geometry might be an ellipse seen under intermediate inclination, which allows us also to reproduce the shadows seen with polarimetric imaging. The uncertainties reported in Table S6 have been estimated by fitting the  $\chi^2$  surface near the fit minimum.

Using equation 1, we can compute the mutual inclination between the orbits and the disk

planes. We find that the angular momentum vector between the inner binary orbit (A-B) and the outer-most ring R1 are misaligned by  $\Phi = 51.1 \pm 1.1^\circ$ . For the outer orbit AB-C, the mutual misalignment is  $\Phi = 38.5 \pm 0.8^\circ$ . The 3-dimensional orientation of the disk planes is illustrated in Figs. S11 (bottom) and S12 (right).

The derived sub-millimeter flux densities allow us to estimate the minimum dust mass in the rings. Assuming that the emission is optically thin, we estimate the dust mass with

$$M_{\text{dust}} = \frac{d^2 F_\nu}{B_\nu(T_d) \kappa_\nu}, \quad (4)$$

where  $F_\nu$  is the sub-millimeter flux density measured with ALMA.  $T_d$  the dust temperature, and  $B_\nu(T_d)$  the blackbody function.  $\kappa_\nu$  is the dust opacity per dust mass, where we adopt  $\kappa_\nu = 0.2(7 \text{ mm}/\lambda) \text{ cm}^2 \text{ g}^{-1}$  (70, 71).

For a viscous accretion disk, (72) showed that the gas temperature (which can be used as proxy for the dust temperature in the thermally coupled case) can be estimated from

$$\frac{c_s}{R\Omega} = H_p/R \quad (5)$$

$$c_s^2 \approx R_g T_d / \mu, \quad (6)$$

where  $c_s$  is the sound speed,  $R_g$  is the universal gas constant,  $\mu$  the mean molecular weight.  $H_p/R$  is the pressure scale height of the disk at radius  $R$ , which we set to 0.05 based on the results of our hydrodynamic simulation and the sharpness of the radial shadows (S1+S2) that we see in the scattered light images.  $\Omega$  denotes the epicycle frequency  $\Omega = \sqrt{GM/r^3}$ . Using a radiative transfer model computed from our SPH simulation, we also validated that this approach provides a reasonable estimate for the dust temperature. The resulting minimum dust masses are reported in Table S6. The mass sum is about a factor 2 lower than the  $0.12 M_\odot$  derived by (36) (combined gas+dust, assuming a gas-to-dust ratio of 100), which is likely due to the much smaller field-of-view, spatial filtering that results from the use of the extended ALMA

configuration (Sect. S1.1.4) and due to flux emission located between and outside the rings that make up  $\sim 30\%$  of the total flux in the image and that is not described by the model. Also, our adopted dust opacities ( $\kappa_\nu$ ) are lower than those used by (36), and therefore our mass estimates are conservative.

### S1.2.6 Disk structure: visible/near-infrared polarimetry

Our four SPHERE and GPI coronagraphic-polarimetric images reveal scattered light originating from the disk surface. The polarized flux is  $\sim 4$ -times higher towards the East than towards the West. Given that polarized intensity images are typically dominated by forward-scattering from dust grains, this indicates that the Eastern side of the disk is facing towards the observer. This conclusion is also supported by CO rotation measurements ((15) and (36)) that show that the Northern part of the disk is receding from the observer (red-shifted). If the disk rotates in retrograde motion (i.e. in clockwise direction on the sky), equivalent to the stellar orbits, then the Eastern side must face towards us.

The emission is inhomogeneous and appears to be arranged broadly in four arcs (A1, A2, A3, and A4; labeled in Fig. 1C), where the drop in polarized intensity between the arcs coincides with the position of the sub-millimeter rings R1, R2 (Figs. 1E and S2, bottom row). We interpret this as a shadowing effect: The rings R1 and R2 might appear bright in sub-millimeter continuum emission due to trapping of mm-sized grains near a pressure maximum, similar to what has been proposed for continuum rings seen in circumstellar disks (e.g. (73)). In this case, we expect an enhanced disk scale height at the radial locations of the sub-millimeter rings, which results in shadowing from the stellar photons in the regions immediately behind the pressure bump (see sketch in Fig. S17). Therefore, these regions appear dimmer in scattered light images.

We see four radial shadows, including two sharply defined shadows extending in South-

East/North-West direction (S1, S2) and two broader shadows extending to the North-East/South-West (S3, S4). To understand the origin of these shadows, we constructed a 3-dimensional scattered light model using the ray-tracing software package Blender (version 2.79c). We include three rings that are set up to resemble ALMA rings R1, R2, and R3 (Table S6). The rings are modeled to be optically thick (i.e. opaque) and vertically extended ( $H/R = 10\%$ ), allowing sharp shadows to be cast on the outer disk.

Inspired by the dust morphologies seen in hydrodynamic simulations (e.g. (4)), we model the region between the rings as warped dust surfaces. To control the warp, the surface is build-up by a tilted ring model. We parameterize the radial profile as a Fermi function in polar coordinates, resulting in a smooth transition between rings of different inclination. Therefore, the inclination of each ring at radius  $r$  follows the slope of the Fermi function  $\sim 1/(e^{-r} + 1)$ . Surfaces are defined by connecting the longitudes on an inner boundary orbit with the equivalent longitudes on an outer boundary orbit. These boundary orbits are allowed to have different values for inclination ( $i$ ), eccentricity ( $e$ ) and longitude of the ascending node ( $\Omega$ ). The surfaces are modeled as geometrically thin scattering surfaces with intermediate optical depth, i.e. they permit some light to propagate through. The detailed optical properties are not essential, as we use the model to simulate shadow morphologies, but do not aim to reproduce the scattered light images quantitatively. We introduce two surfaces in our model, where the first surface connects rings R1 and R2 and is not significantly warped. The second surface connects R2 with an inner truncation orbit (in the following referred to as 'break orbit'), where the warp is truncated.

The free parameters to define the 3-dimensional shape and orientation of R3 are the inclination  $i_{R3}$ , eccentricity  $e_{R3}$ , and argument of periastron  $\Omega_{R3}$ . We make use of the fact that we need to match simultaneously the shadow pattern (seen in our SPHERE and GPI images) as well as the on-sky projected shape of the occulting ring R3 (seen by ALMA), which allows us to fix  $a_{R3} = b_{R3}/\sqrt{1 - e_{R3}^2}$  and  $\omega_{R3}$  based on the three aforementioned parameters.

We compute synthetic images with ray-tracing, convolve them to match the resolution achieved by our SPHERE/GPI observations, and adjust the free model parameters in order to obtain the best match on the direction and shape of the shadow patterns between the model and our scattered light imagery (Fig. 1C, 1D). We are able to roughly reproduce the shape of the apparent ellipse shape that is formed by the scattered light arcs A3 and A4 (Fig. 1C). The orientation of this apparent ellipse (with semi-major axis oriented along  $PA \sim 60^\circ$ ) differs significantly from the orientation of the outer disk ( $\Omega_{R2} = 180 \pm 4^\circ$ ). Our scattered light model allows us to reproduce this shape approximately by choosing the following parameters for the break orbit:  $a_{\text{break}} = 90 \text{ au}$ ,  $e_{\text{break}} = 0.65$ , and  $\Omega_{\text{break}} = 60^\circ$ . Choosing an inclination value  $i_{\text{break}} = 15^\circ$  allows us then to reproduce the prominent arc A3 as scattered light from the side of the warp that is facing away from us and that is directly illuminated by the stars (see sketch in Fig. S17). The much dimmer arc A4 corresponds to light from the warp surface that is facing towards us, where we see only the self-shadowed outer side of the warp that is not directly illuminated. The highest column density in the warp is towards the North-East and South-West, matching the directions where we see the broad shadows S3 and S4 (see Fig. 2A).

The derived parameters for ring R3 are listed in Table S6 and show that ring R3 is significantly eccentric ( $e_{R3} = 0.3 \pm 0.1$ ), which is consistent with the off-center position of the ring with respect to the stars. As the ring is significantly inclined with respect to the plane of the sky, it casts a narrow radial shadow, both in South-East direction (matching S1) and North-West direction (matching S2). The model can reproduce the radial curvature seen in shadow S1 as a geometric effect, where the shadow cast by R3 is projected onto the warped surface. The inner part of the shadow ( $S1_{\text{inner}}$ ) is projected on the warped surface, while the outer part ( $S1_{\text{outer}}$ ) is projected on the non-warped surface connecting R1 and R2.

An interactive 3-dimensional model that illustrates the deduced disk geometry can be found in Fig. S18.

### S1.2.7 Locating accretion-tracing Br $\gamma$ emission

The system shows signposts of active accretion, including Br $\gamma$  line emission (57) and strong UV veiling ( $\dot{M}_{\text{acc}} \approx 3 \times 10^{-7} M_{\odot} \text{ yr}^{-1}$ ; (74)). Our CRIFES spectro-astrometry constrains the spatial origin of the Br $\gamma$  accretion tracer line. Figure S3 (right) shows that the line emission originates from close to the position of the tertiary (C) component, while the accretion onto the primary/secondary is negligible, within the achieved measurement precision ( $(\dot{M}_{\text{acc}}^{\text{A}} + \dot{M}_{\text{acc}}^{\text{B}}) \lesssim 20\% \cdot \dot{M}_{\text{acc}}^{\text{C}}$ ). This finding supports theoretical models that predict the outer component in multiple systems to disrupt the accretion stream onto the primary and channel most of the infalling material onto the circumsecondary disk, effectively limiting the mass that the primary can accrete (e.g. (75, 76)).

The higher accretion rate measured towards the tertiary is also compatible with the higher dust column density (sub-millimeter flux) measured towards component C than components A+B (Figs. 1B and S16).

## S1.3 Hydrodynamic modeling

Using our unique constraints on the 3D orbits and stellar masses, we conducted SPH simulations of the GW Ori system. Our simulations were performed using the SPH code by (77), (78), and (79) that has already been applied to study hydrodynamic effects in higher-order multiple systems (e.g. (78)) and protoplanetary disks (e.g. (80)). The simulation setup is based on our actually measured stellar orbits and the GW Ori stellar and disk parameters listed in Table S3.

To initialize the sink particles in the SPH simulation we need to obtain instantaneous positions and velocities of the stars. For this purpose, we calculate the initial positions and velocities at JD 2456674.8, i.e. the point in time when GW Ori B passes through periastron and has a true anomaly of  $0^\circ$ . The periastron passage of GW Ori C occurred JD 2815.2 earlier so we solve the Kepler equation to obtain the true anomaly of GW Ori C JD 2815.2 after periastron passage.

In the SPH and radiative transfer models we define the positive  $\hat{x}$  and  $\hat{y}$  directions as North and East respectively. The  $\hat{z}$  axis points towards the observer. We perform a rotation to position the stars in the model coordinates. The orbital elements  $\Omega$ ,  $i$  and  $\omega$  loosely correspond to the Euler angles  $\alpha$ ,  $\beta$  and  $\gamma$ , but need to be adjusted to account for differences in their definitions.

The longitude of the ascending node,  $\Omega$ , is measured anti-clockwise from North to the point where the orbital plane intersects the plane of the sky and the motion of the secondary is away from the observer, into the sky. Mathematically, the ascending node is defined as the node where the motion has a positive  $\hat{z}$  component. This is the opposite node to the astronomical definition so we set  $\alpha = \Omega - \pi$  radians. The inclinations listed in Table S6 are measured at the ascending node, clockwise looking down the ascending node. Since  $\beta$  is measured anticlockwise around the opposite node,  $\beta = i$ . In Table S5, the visual binary conventions are used for defining  $\omega$ . Accordingly,  $\omega$  is measured in the direction of motion of the companion from the ascending node of the secondary and so  $\gamma = \omega$ . We can then apply standard Euler rotations about  $z - x' - z''$ , with negative rotation angles, in the order  $-\gamma$ ,  $-\beta$ ,  $-\alpha$ , since we move from the frame of the orbit to the frame of the sky.

To initialize the stellar positions and velocities we use the following strategy: The system is considered as a hierarchical triple with motion of A and B relative to their mutual center-of-mass and the motion of C and the A-B center-of-mass are treated separately. The positions are calculated in the frame of the orbits from the true anomaly and the barycenter distance found from the stellar masses. The position vectors are then rotated to the sky orientation as described above and the positions of A & B are shifted relative to the A-B center-of-mass calculated from the orbit of C. The relative velocities are calculated, again, first in the frame of the orbits according to the standard formulae for an elliptical orbit and then scaled for the component mass. The velocity vectors are then rotated onto the frame of the sky and the velocity of the A-B center-of-mass due to C is added to the velocity of A and B. The disk is positioned by

following a similar rotation but excluding the  $-\gamma$  rotation since it is initially axisymmetric.

To model the disk we use  $8 \times 10^5$  SPH gas particles. We begin with a disk that has a 200 au outer radius and a 20 au inner radius. The surface density profile follows  $\Sigma(r) \propto r^{-1/2}$ , with a scale-height given by a fixed  $H_p/R = 0.05$ . We do not model the outer part of the observed disk because we are primarily interested in the studying the warping and/or disk tearing of the inner disk and only modeling the inner 200 au reduces the computational expense. We set up the SPH particles in a Keplerian disk orbiting a single gravitational mass of  $5.26 M_\odot$  (i.e. the total stellar mass of the system), and the disk is evolved until any transient structures from the initial conditions have dissipated. We then add the three stars as point masses (sink particles with accretion radii of 1 au), and reorientate the settled disk to match the orientation inferred from observations. We also remove any disk material within 40 au of the center-of-mass of the stellar system. This gives the initial conditions for our hydrodynamical simulation. We run the simulation without self-gravity of the gas, and we exclude the gravitational force from the disk on the stars so that the orbital parameters of the stellar system stay as close as possible to those that are observed throughout the simulation.

Once the hydrodynamical simulation is started, the inner region of the disk slowly develops a warp over the first 1000–3000 years and the inner edge spreads inward. At around 5500 years an inner ring starts to develop and detaches from the rest of the disk. Its initial radius is approximately 30 au. It precesses rapidly and from about 6500 years onward it is distinct from the rest of the disk. Over the next 3000 years, the precessing ring occasionally interacts with the inner edge of the warped outer disk, accreting gas, growing in radius, and becoming more eccentric. At 9500 years, the time shown in Fig. 3 of the main paper, the inner ring has a radius of approximately 40 au and an eccentricity of  $\sim 0.2$ , and the outer part of the disk is warped. These structures are in qualitative agreement with those that are observed for the GW Orionis system.

Using the 3-dimensional gas density profile derived from our SPH simulation we then computed synthetic images for the 1.3 mm dust continuum using the TORUS radiative transfer code (81). For the radiative transfer simulation we took the disk mass to be  $0.1 M_{\odot}$ , and assumed a fixed gas-to-dust ratio of 100. We adopt silicate grain opacities (82) with a grain size distribution  $a^{-3.5}$  and  $0.1 \mu\text{m} \leq a \leq 10 \mu\text{m}$ . The radii and effective temperatures of GW Ori A, B, and C were taken to be  $4.5 R_{\odot}$ ,  $2.8 R_{\odot}$ ,  $2.8 R_{\odot}$ , and 5400 K, 4640 K, 4640 K respectively, based on the Pisa stellar models (83) and adjusted to better match the SED presented in (24).

Although the hydrodynamical simulation is not a perfect fit to the observed system, it displays all of the features that we have used to model and explain the observations including disk tearing, the formation of an inner, precessing, eccentric ring that has similar dimensions to the observed inner ring, and a warped outer disk. With the differential precession that naturally occurs in the hydrodynamical model it is likely to be difficult to get an exact match with the observations. Furthermore, parameters such as the exact scale-height and mass of the disk and its viscosity are unknown. We plan to explore the dependence of the structures produced in the simulations on the poorly constrained parameters with additional hydrodynamical calculations in the future, but this extended study is beyond the scope of this paper.

We note that some hydrodynamic simulations of misaligned multiples find that disk tearing can result in a set of multiple nested rings (e.g. (4)), which opens the possibility that the drop in sub-millimeter flux that we detect between the two outer-most dust rings (between R1 and R2) might also be related to disk tearing. Alternatively, it is possible that this gap represents only a depletion in large dust grains, which could indicate the action of radial dust drift and dust filtration effects induced by the strong density gradient near the inner edge of R2 (84). Alternatively, the dust gap might be accompanied by a depletion in gas density, which could indicate the presence of gap-opening planets located within the gap. Answering this question

is out of the scope of this study, but could be addressed with dedicated new hydrodynamic simulations incorporating decoupled gas-dust species, grain growth, and with higher resolution to capture a wider range of disk radii.

## S2 Supplementary Text

### S2.1 Analytic disk tearing considerations

The strongly misaligned eccentric ring R3 detected by our sub-millimeter imaging shows many characteristics that are predicted for disk tearing. For a quantitative comparison with earlier theoretical predictions, we compare the measured R3 radius to analytic estimates of the break radius  $r_{\text{break}}$  that is defined as the point where the external torque exerted by the misaligned binary exceeds the internal torque due to pressure forces (4, 5):

$$r_{\text{break}} \lesssim 50 \mu_C^{1/2} |\sin 2\Phi|^{1/2} \left( \frac{H_p/R}{0.1} \right)^{-1/2} \left( \frac{\alpha}{10^{-3}} \right)^{-1/2} a, \quad (7)$$

where  $\mu_C = M_C/(M_A + M_B + M_C)$  is the mass fraction of the tertiary,  $\Phi$  is the initial misalignment between the disk and the binary ( $\Phi = 51.1 \pm 1.1^\circ$  for the AB-C system; Sect. S1.2.5),  $H_p/R$  is the pressure scale height of the disk, and  $\alpha$  the viscosity.

As this equation has been derived for misaligned binary systems, it has to be applied with caution to a triple system such as GW Ori. However, we expect the torque on the outer disk to be dominated by the wide-separation tertiary and therefore apply the estimate to the AB-C system. Adopting  $H_p/R = 0.05$  (Sect. S1.2.5), we find that the break radius estimate matches the size of the R3 semi-minor axis ( $b_{\text{R3}} = 43$  au) for  $\alpha \lesssim 0.05$  (or any case where the product  $\alpha \cdot H_p/R \lesssim 0.0025$ ). As most estimates for the  $\alpha$  viscosity in protoplanetary disks range between 0.001 and 0.04 (85), we conclude that the disk around GW Ori is indeed likely susceptible to disk tearing at the location of ring R3.

## S2.2 Origin of the photometric variability in GW Ori

Quasi-periodic eclipse events and photometric variability are commonly observed towards young stellar objects. GW Ori shows very interesting evidence for temporal variability: It is known to exhibit semi-regular, Algol-like photometric dimming events at visible wavelengths (86, 87, 15). In total, 15 eclipse events have been reported for the period between 1998 and 2016, with typical occultation depths of 0.1-0.7 mag in visible light (15) and durations between 10-50 days. The origin of these eclipses is puzzling, in particular considering the rather face-on orbit orientation of the inner binary system (14, 15). (15) found that the eclipses occur preferentially between phases 0.4-0.8 from periastron of the tertiary orbit, but noted this correlation might be due to seasonal sampling of the data. Furthermore, (15) reported a smooth 0.2 mag amplitude modulation that is phased with the AB-C orbital period and that results in highest V-band flux near periastron (phase 0). The authors suggested that this modulation might indicate that the A-B binary is partially obscured by a circumtriple disk when the tertiary is at apoastron (corresponding to the time when A-B is furthest East). Finally, (24) noted that the spectral energy distribution (SED) of GW Ori exhibits dramatic changes on timescales of  $\sim 20$  yrs in the near/mid-infrared spectral range, suggesting that highly dynamical processes are taking place in the inner disk environment.

Our spatially resolved observations provide the following pieces of evidence to understand the origin of the variability:

**Variable extinction in the inner binary:** We find that the relative contributions of the three stars to the total near-infrared flux changes dramatically between the 12 epochs covered by the IOTA, VLTI, and MIRC-X data (Table S4), to the extent that the lower-mass secondary (B) is at some epochs brighter than the primary (A), as indicated by the measured strong and highly significant flux ratio variations ( $0.64 \lesssim F_B/F_A \lesssim 1.12$ ). In Fig. S14 (left) we plot the  $F_B/F_A$  flux ratio as function of the phase of the A-B binary. We do not see a clear correlation between

the flux ratio variations and the orbital phase. We suggest that this variability is due to extinction caused by optically thin,  $\mu\text{m}$ -sized dust streaming on out-of-plane orbits towards the inner binary, crossing the line of sight randomly.

**Replenishment of a circumtertiary disk near periastron and apoastron passage:** Besides the inner-binary variability, we also observe strong variability in the contributions of the C component ( $0.15 \lesssim F_C/F_A \lesssim 0.47$ ) that seem to be correlated with the orbital period of the tertiary: Fig. S14 (right) shows that the relative contributions of the tertiary to the total photospheric flux doubles near periastron passage (phase 0). The contributions are also 40% higher near the apoastron passage of the tertiary (phase 0.5). This phase-locked variability in the tertiary flux ratio can be explained with dust that is strip away from the circumbinary disk (R4) near periastron passage, and from a circumtriple disk near apoastron passage. This dust replenishes a circumtertiary disk ( $D_C$ ) that radiates prominently in the near-/mid-infrared, causing the observed near-infrared excess near phase 0 and phase 0.5 (Fig. S14, right). The excess emission is stronger near periastron, indicating that more material is accreted at this part of the orbit. As the tertiary moves away from periastron/apoastron, this dust reservoir is depleted. This scenario is also supported by our detection of accretion signatures on the tertiary at the time of our CRIRES observations (Sect. S2.3 and Fig. S3). These observations were obtained near apoastron passage of the tertiary (phase 0.56; Sect. S1.2.7). Furthermore, our L-band aperture masking observations were obtained close to apoastron passage (phase 0.65) and indicate L-band thermal dust emission North-East of the tertiary (Sect. S1.2.4), possibly tracing a dust flow from a circumtriple disk onto the circumtertiary disk. Finally, the dynamic interaction of the tertiary with a circumtriple disk near apoastron passage could kick material out of the disk plane, thereby causing the increased line-of-sight extinction towards the tertiary that is required to explain the 0.2 mag V-band amplitude modulation observed by (15).

**Variable shadowing on the outer disk:** Our GPI (J- and H-band) and SPHERE (H-band) scattered light images were recorded at epochs separated by 316 days, namely on 2018 January 4 and 2018 November 16. The images from both epochs show overall similar morphologies, but there are notable differences (Fig. S19): Most notably, the Northern part of the innermost arc A1 appears brighter in the SPHERE image than in the GPI image ( $PA \sim 70 \dots 110^\circ$ ). Therefore, we suggest that an occulter has moved between the two epochs in clockwise direction, causing the variable illumination that we see in the scattered-light images. As most likely candidate for the occulter we identify the circumtertiary disk ( $D_C$ ). Any shadow cast by  $D_C$  should move in clockwise direction, matching the rotation direction needed to explain the variability seen in the scattered light images. From the best-fit orbit solution, we compute that the tertiary was located at position angle  $\theta_{AC} = 113^\circ$  with respect to the primary at the epochs of the GPI images, which allowed the circumtertiary disk to cast a shadow in Eastern direction. By the time of the SPHERE observations, the tertiary moved to  $\theta_{AC} = 59^\circ$ , allowing the Eastern part of the disk to be directly illuminated and to appear brighter in the SPHERE image. The direction of potential shadows cast by the circumtertiary disk  $D_C$  are indicated with arrows in Fig. S19.

The location of the radial shadows (S1, S2) has not changed between the two epochs of our scattered-light imaging, which is consistent with the predicted, relatively long precession timescale of the broken ring R3 ( $\sim 8,000$  years; Sect. S1.3). The motion of a precessing ring would be directed in opposite direction than the orbital motion, and an associated shadow should therefore rotate in anti-clockwise direction.

**Circumbinary disk (R4) as possible occulter:** Even though our existing data puts only weak constraints on the 3-dimensional orientation of the circumbinary disk, we suspect that R4 might be responsible for the observed quasi-period eclipse events ((86), (87), (15)) as the

Keplerian dynamical timescale at its location matches roughly the 1-2 year repetition cycle of these eclipses. (15) found no correlation between the occurrence of the eclipses and the A-B nor AB-C orbit, which could indicate that the obscuring ring follows a more complex nodding or precession motion. The constant, out-of-plane torque acting on ring R4 from the misaligned A-B and AB-C orbits could lead to differential precession. Dedicated SPH simulation with high resolution will be needed to simulate this effect, as the simulations shown in Sect. S1.3 are optimized to simulate disk tearing on scales of a few tens of astronomical units and analytic estimates for the precession timescale (e.g. (88, 89)) do not apply given that R4 is perturbed by an internal (A-B) and external perturber (AB-C).

### **S2.3 Site of active accretion and evidence for phased accretion in GW Ori**

By inducing oscillations in the disk tilt and pushing the disk eccentricity (22, 23) disk tearing can increase the accretion rate by up to an order of magnitude (4), which has important implication for our understanding of disk evolution. Our images show dust that might be part of the accretion flow feeding the central triple system, namely the filamentary structures that we see inside of ring R3 in scattered light ( $F_{\text{scat}}$ ). GW Ori shows signs of ongoing active accretion through hydrogen recombination line emission, with an estimated accretion rate of  $\sim 3 \times 10^{-7} M_{\odot}/\text{yr}$  (74). We conducted spectro-astrometric observations in the hydrogen  $\text{Br}\gamma$  transition that allow us to localize the sites of active accretion (AB-C orbital phase 0.56; Fig. S3). The tertiary was near the apoastron position on its highly eccentric orbit ( $e=0.379 \pm 0.003$ ) and we find that the accretion occurred predominantly on the tertiary ( $\dot{M}_{\text{acc,C}} \gtrsim 5 \cdot (\dot{M}_{\text{acc,A}} + \dot{M}_{\text{acc,B}})$ ). Furthermore, our near-infrared interferometric monitoring measured infrared ( $2 \mu\text{m}$ ) excess emission at the position of the tertiary near periastron and apoastron passage (Sect. S1.2.1 and Fig. S14). This phase-dependent infrared excess emission could indicate that the circumtertiary disk is replenished with dust from the circumbinary

disk (R4) and from a circumtriple disk when the tertiary approaches the innermost / outermost point on its orbit. Dust emission from the circumtertiary disk is also seen in our submillimeter imaging (component  $D_C$ ) and in  $3.5\ \mu\text{m}$  aperture masking interferometry observations (Sect. S1.2.4 and Fig. S15). As the tertiary moves away from periastron/apoastron the dust in the circumtertiary disk is quickly depleted, resulting in reduced infrared excess. This finding supports theories for pulsed accretion in eccentric multiple systems (90) and also confirms a previously-postulated dynamical effect where most of the accretion stream is channeled onto the lowest-mass component in binary systems, effectively limiting the mass that the primary can accrete (75, 76).

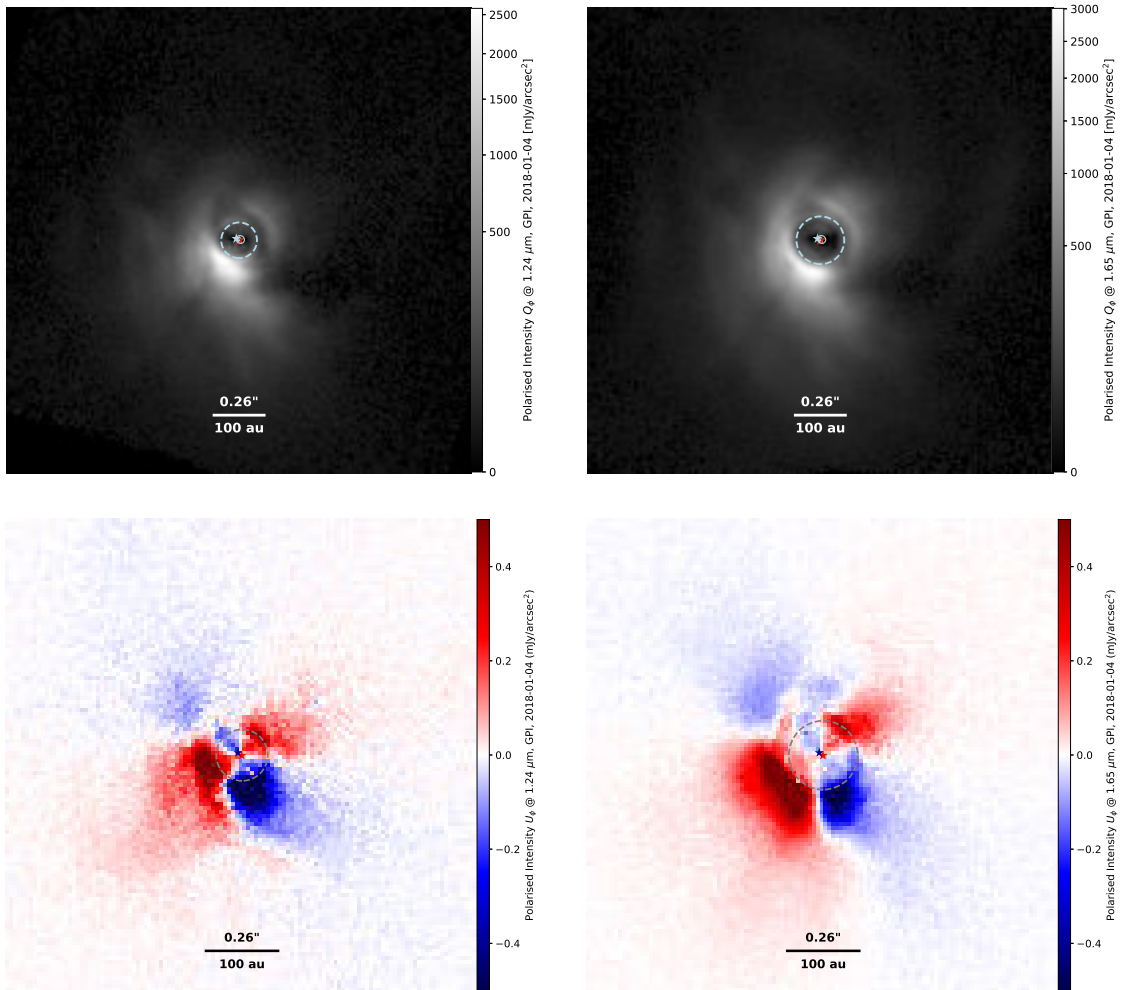


Figure S1 – Polarized intensity image for Stokes  $Q_\phi$  (top row) and  $U_\phi$  (bottom row) retrieved with GPI in J-band (left) and H-band (right).

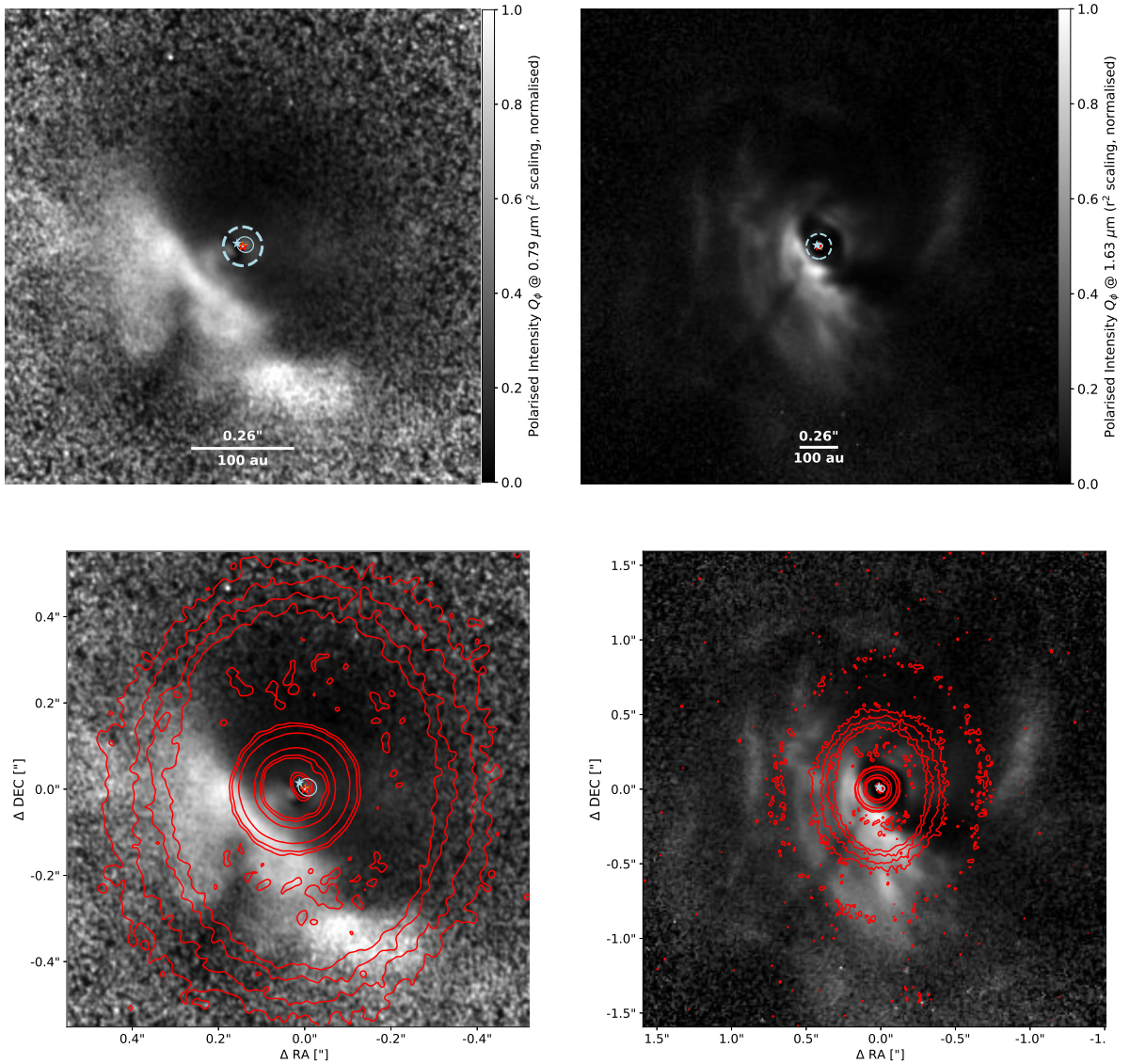


Figure S2 – Polarized intensity  $Q_\phi$  images recorded with SPHERE/ZIMPOL (left) and SPHERE/IRDIS (right). Both images have been scaled with  $r^2$  to emphasise structures in the outer disk, where  $r$  is the distance from the star. In the top row we also indicate the inner working angle of our observing setup with a dashed blue circle, marking the region where the imaged structures are affected by residual star light contributions (for ZIMPOL) or the coronagraphic mask (for IRDIS). In the bottom panel, we overlay the images with the ALMA image as contours. In all panels, we also indicate the position of the stars at the epoch of the observation (as derived from our best-fit orbit solution) and the orbit of the tertiary component.

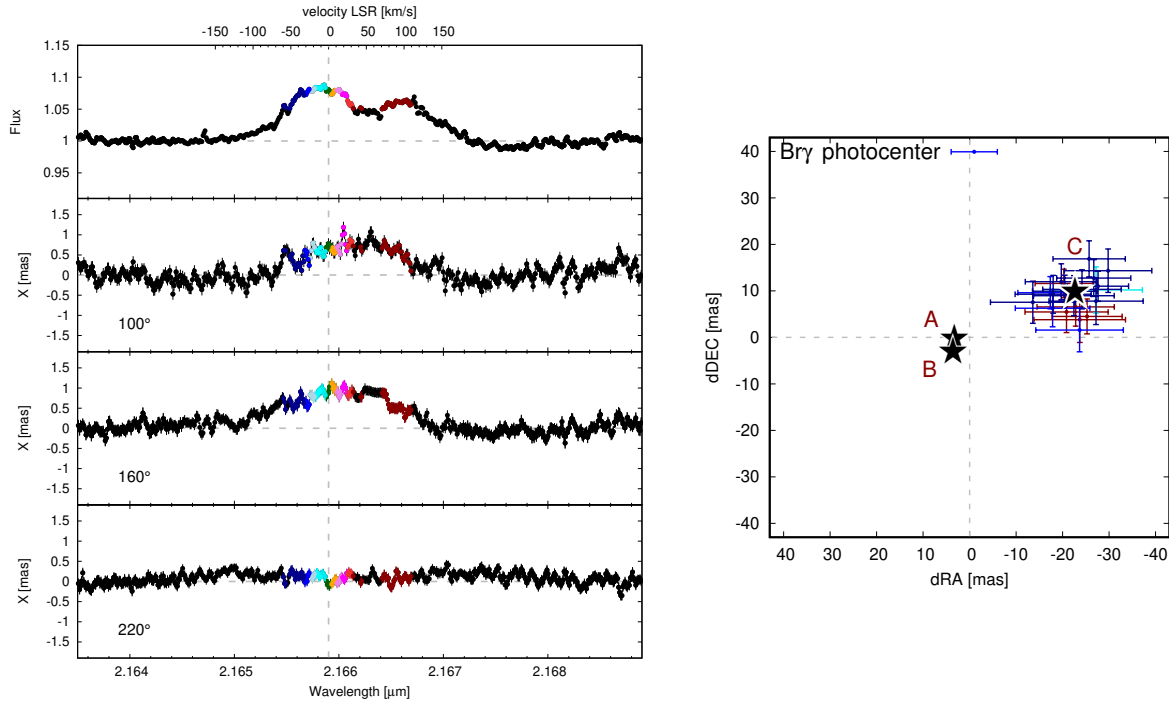


Figure S3 – Photocenter measurements constraining the origin of the accretion-tracing hydrogen  $\text{Br}\gamma$  line emission with respect to the continuum photocenter. The observation has been obtained near the apoastron position of the tertiary (AB-C phase 0.56). Left: CRIFRES spectrum (top) and spectro-astrometric signal  $X$  derived towards three different position angles (2nd panel from top:  $100^\circ$ ; 3rd panel:  $160^\circ$ ; bottom panel:  $220^\circ$ , and anti-parallel slit angles). Right: Continuum-corrected photocenter offsets derived from the CRIFRES spectro-astrometry, where the color points indicate the photocenter displacement in the blue/red-shifted line wing (the origin of the coordinate system corresponds to the continuum photocenter). The star symbols indicate the position of the three stars at the epoch of the CRIFRES observations in 2012 November 11, as computed from our best-fit orbit solution.

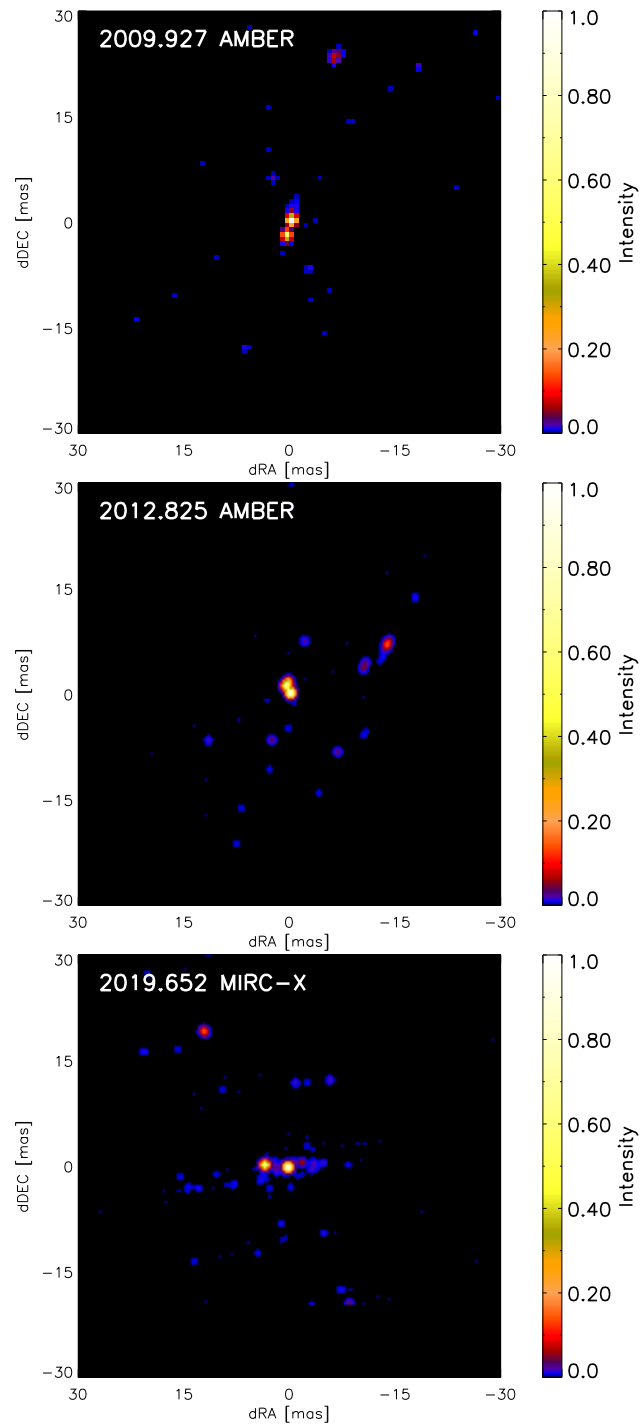


Figure S4 – Aperture synthesis images derived from some of our AMBER and MIRC-X observations.

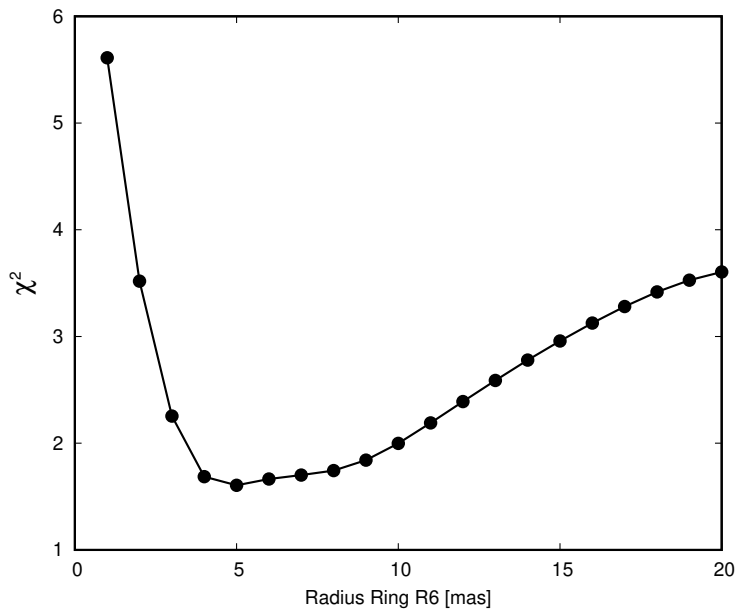


Figure S5 – Goodness-of-fit indicator ( $\chi^2$ ) for different ring radii for the near-infrared-emitting ring R4, obtained by fitting all IOTA, AMBER, and MIRC-X data simultaneously.

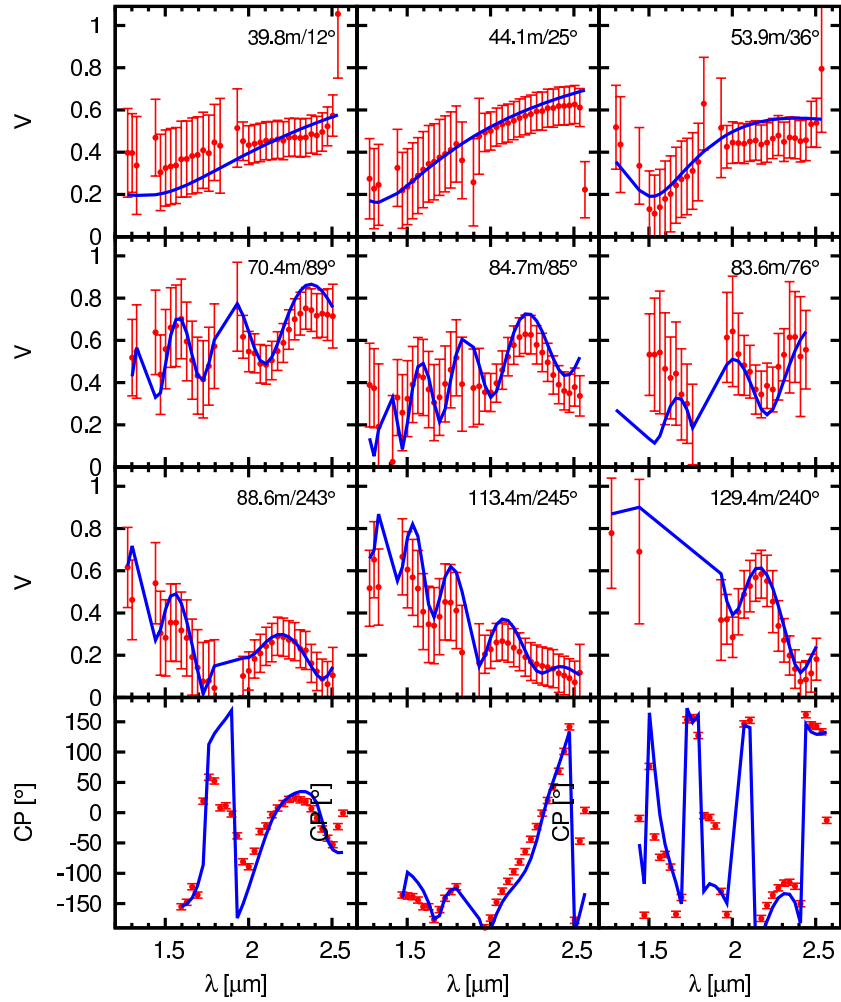


Figure S6 – VLT/AMBER GW Ori data recorded on 2012 October 29 (data points) at three hour angles (three columns) with the UT configuration UT1-UT2-UT4. The visibilities (top three rows) and closure phases (bottom row) are over-plotted with the triple star +smooth ring model outlined in Sect. S1.2.1 (solid curves).

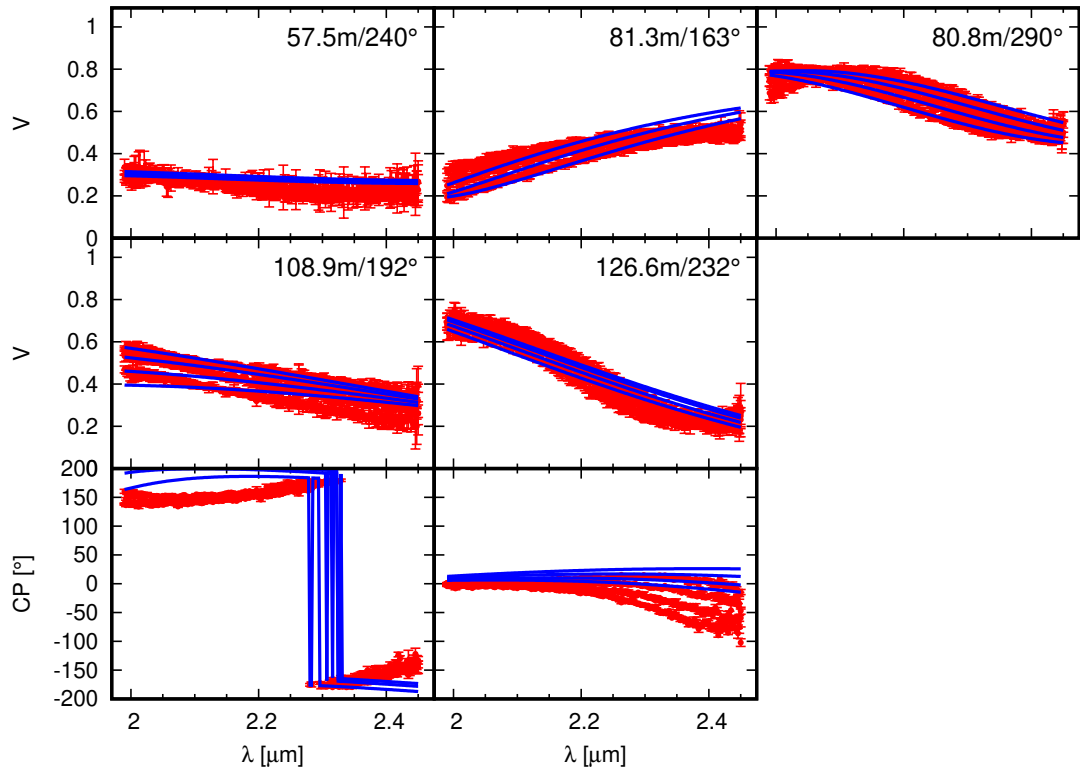


Figure S7 – VLT/GRAVITY data recorded on 2018 February 5 (data points) with the AT configuration A0-G1-J2-J3. The visibilities (top three rows) and closure phases (bottom row) are over-plotted with the triple star +smooth ring model outlined in Sect. S1.2.1 (solid curves).

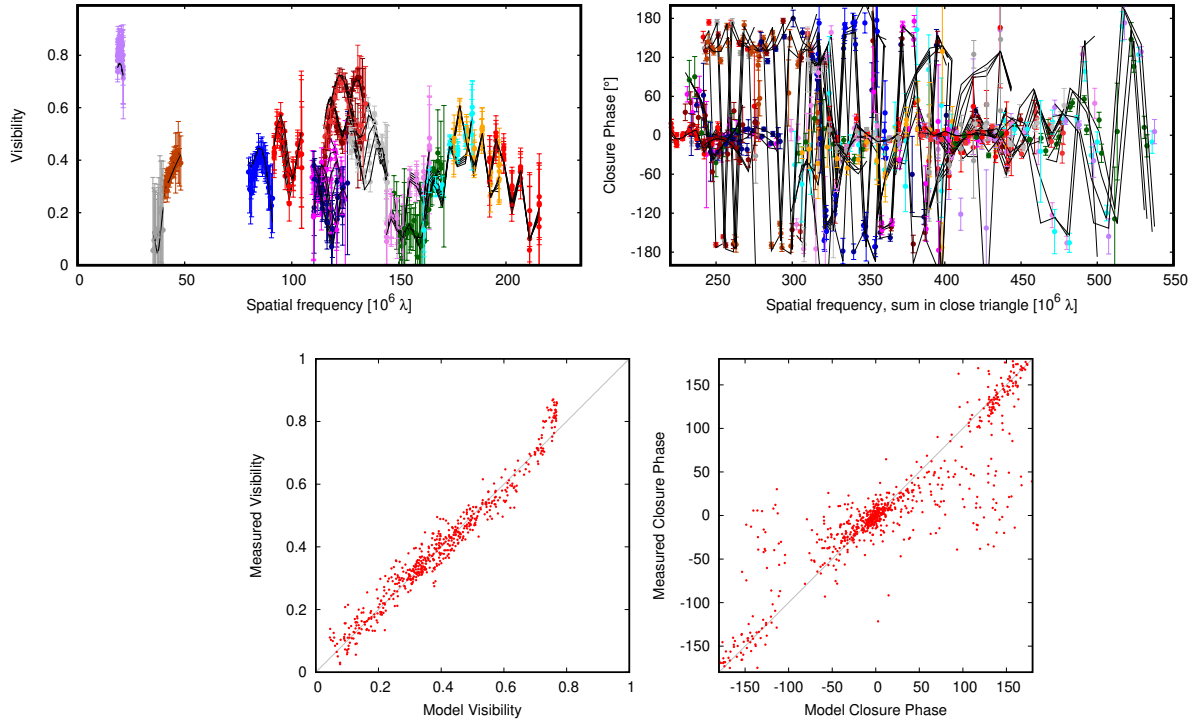


Figure S8 – MIRC-X data recorded on 2019 August 27 (data points) with the 6-telescope CHARA array. The visibilities (left) and closure phases (right) are over-plotted with the triple star +smooth ring model outlined in Sect. S1.2.1 (solid curves). The top row shows the data plotted as function of spatial frequency, while the bottom shows the measured observables plotted versus the model values.

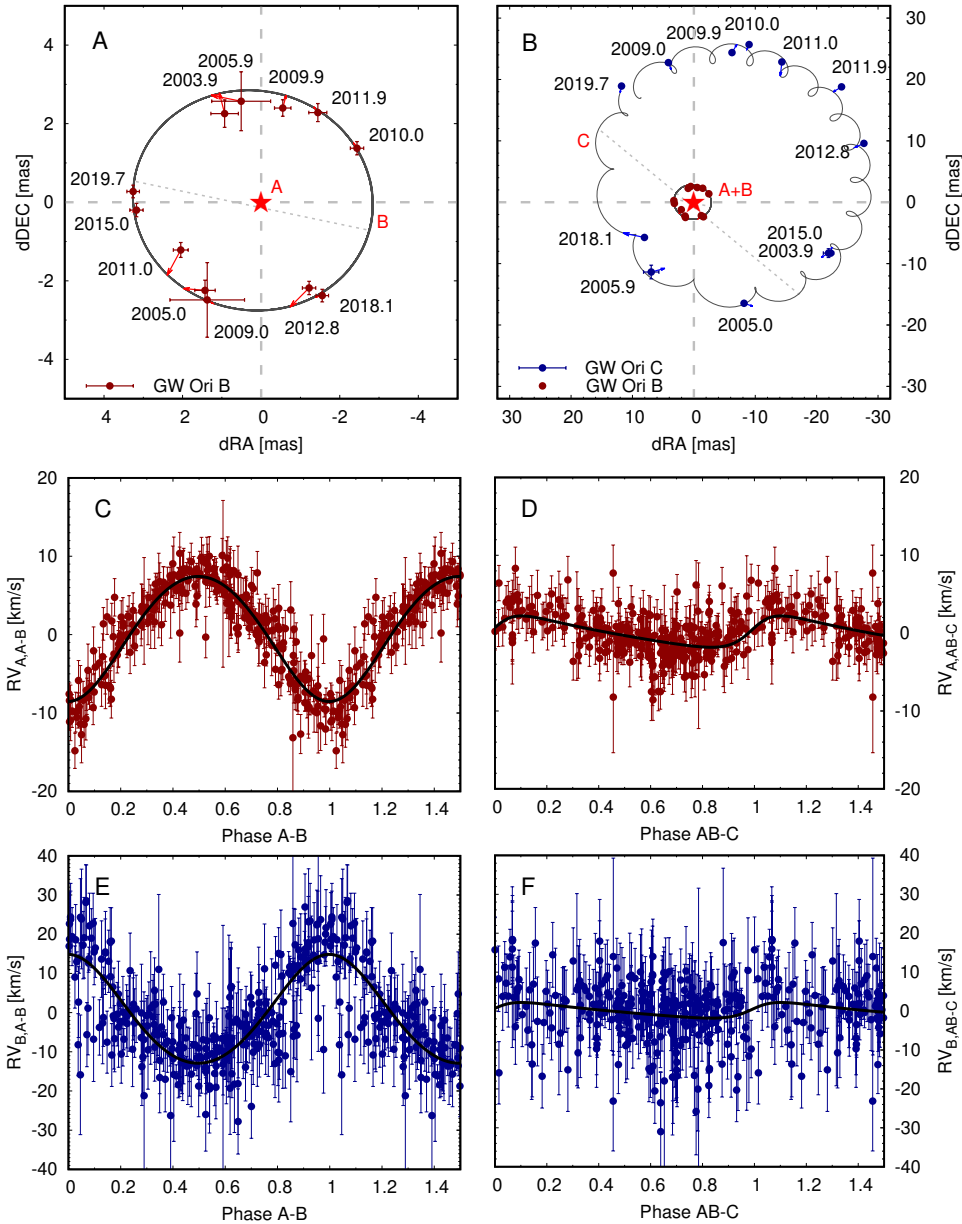


Figure S9 – (A)+(B): Astrometry measurements of the GW Orionis inner short-period binary system A-B (panel A) and long-period system AB-C (panel B), centered on primary A. Over-plotted is our best-fit orbit solution (solid lines) and the line of nodes (dashed lines). (C)+(D): Radial velocity variation measured in photospheric lines associated with the primary (RVA) after subtracting the motion due to the AB-C orbit (panel C) and to due to the A-B orbit (panel D), respectively (data from [Czekala+2017]). We over-plot the best-fit model that describes the motion of the A-B (panel C) and AB-C system (panel D). (E)+(F): Radial velocity variation measured in photospheric lines associated with the secondary (RVB) after subtracting the motion due to the AB-C orbit (panel E) and to due to the A-B orbit (panel F). Again, we overplot with the best-fit model that describes the radial velocities corresponding to A-B (panel E) and AB-C (panel F).

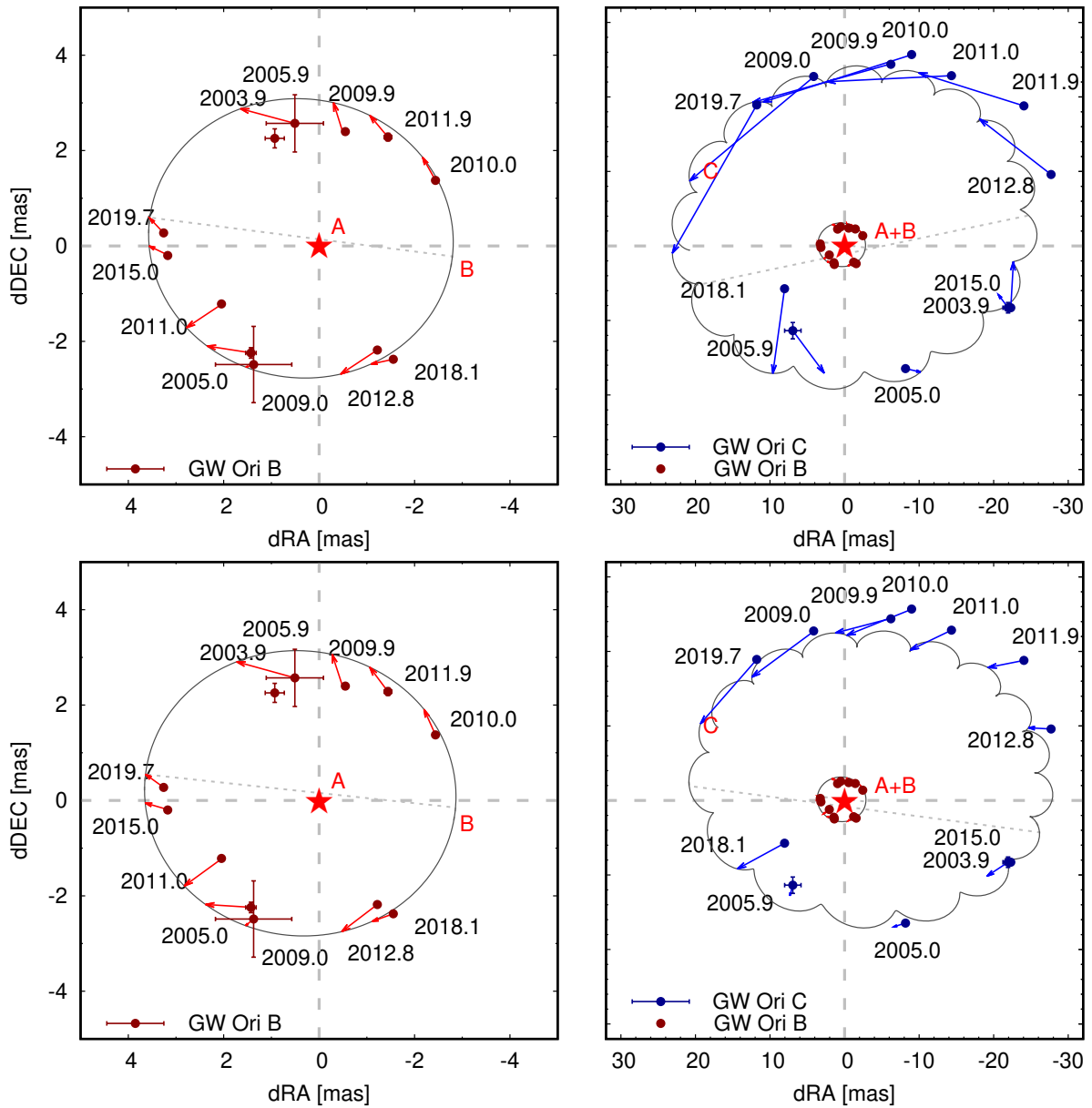


Figure S10 – The astrometry predicted by the two orbit solutions in (15), overlotted on the new data.

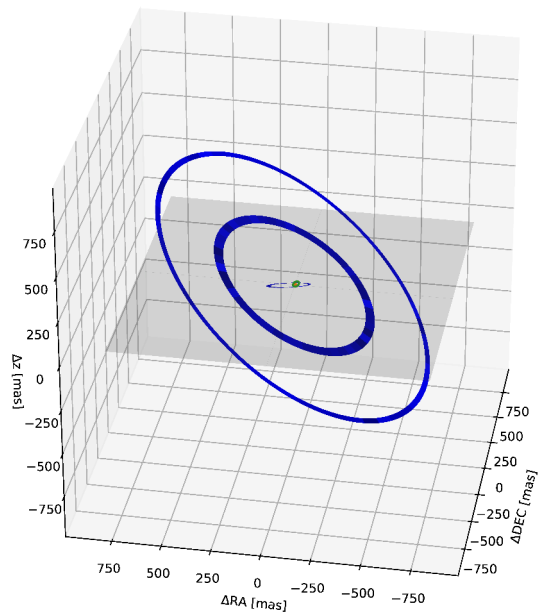
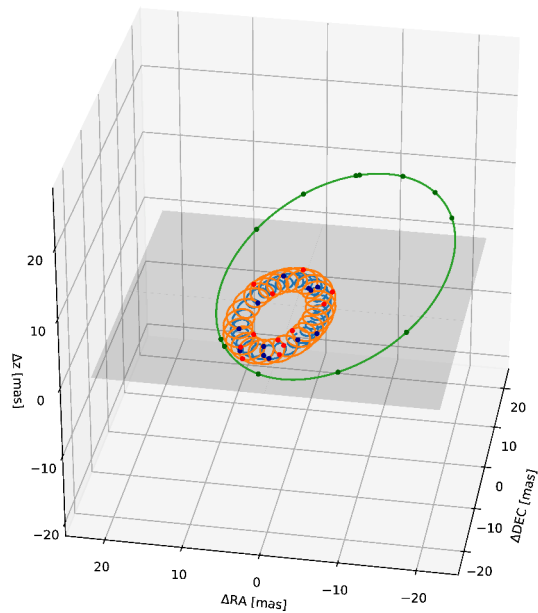


Figure S11 – 3-dimensional orientation of the stellar orbits (A: blue curve; B: orange curve; C: green curve) and the brightest sub-millimeter rings R1, R2, and R3 (blue rings). The origin of the plots represents the center-of-mass of the system. The grey surface represents the plane of sky.

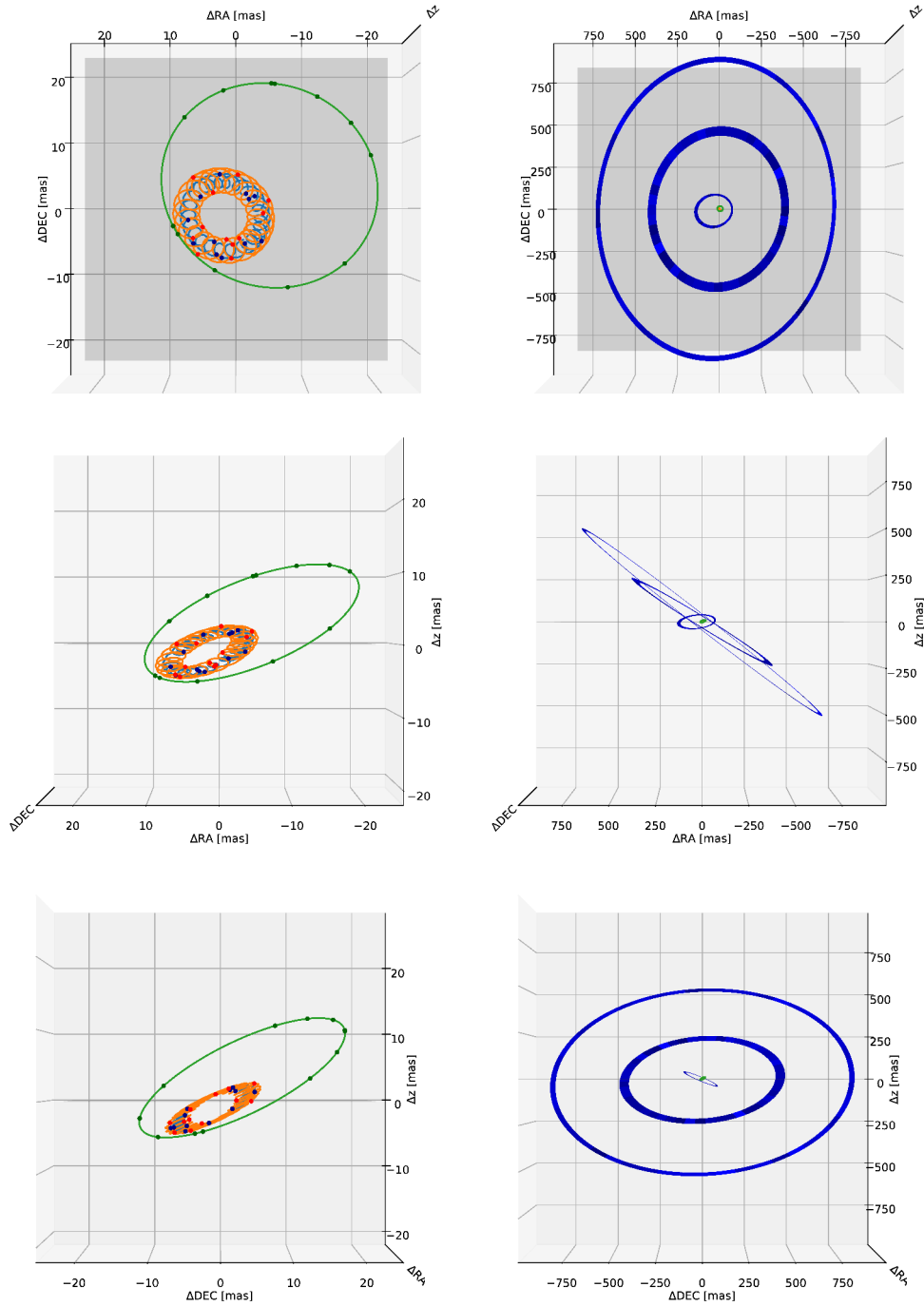


Figure S12 – 3-dimensional orientation of the stellar orbits (A: blue curve; B: orange curve; C: green curve) and the brightest sub-millimeter rings R1, R2, and R3 (blue rings). The origin of the plots represents the center-of-mass of the system. Top: On-sky projection; Middle: View from South; Bottom: View from East. Positive values on the  $\delta z$  axis point towards the observer. The left and right row represent two different spatial scales. The points in the orbit curves indicates the position of the components at the times when our astrometric observations were recorded.

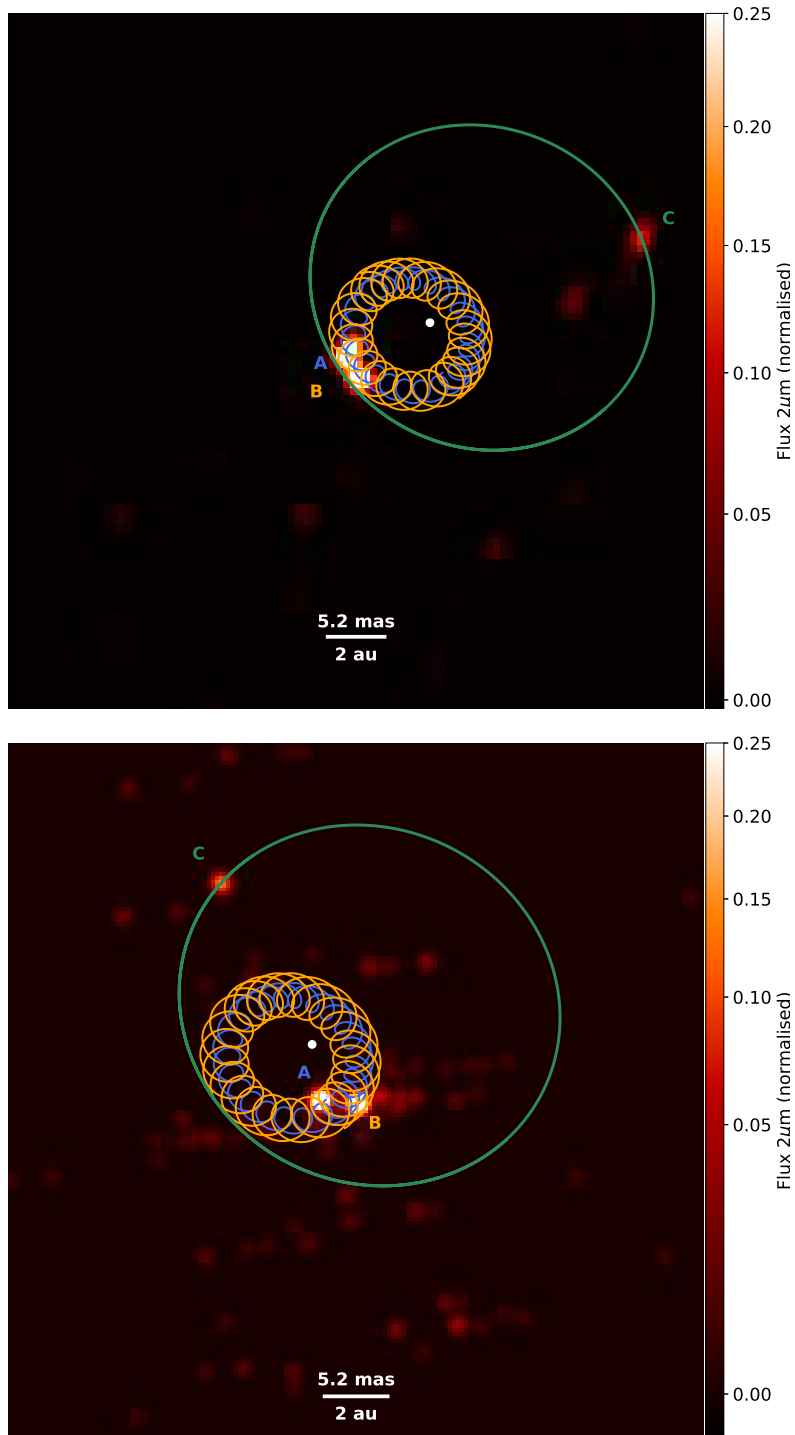


Figure S13 – Aperture synthesis images derived from our AMBER 2012 October 29 (top) and MIRC-X 2019 August 27 observations, overplotted with the best-fit orbit solution. The plot is centered on the center-of-mass of the system.

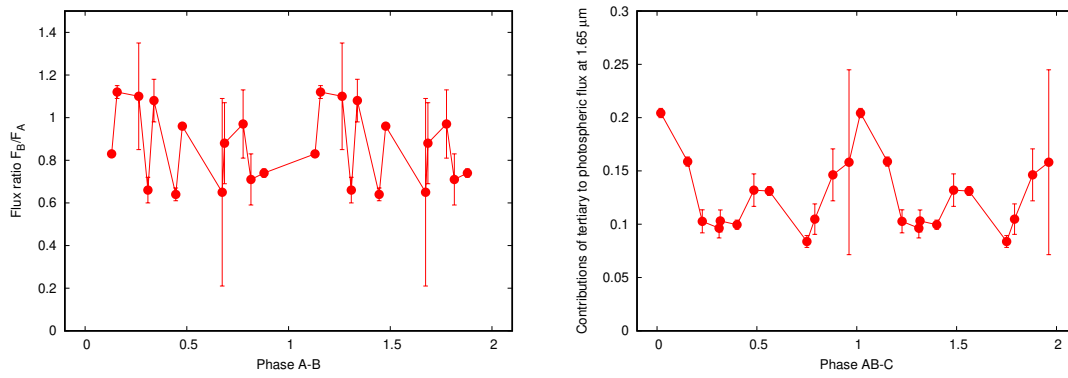


Figure S14 – *Left:* Flux ratio of the primary/secondary, plotted as function of phase of the inner binary. *Right:* Relative contribution of the tertiary to the total photospheric flux.

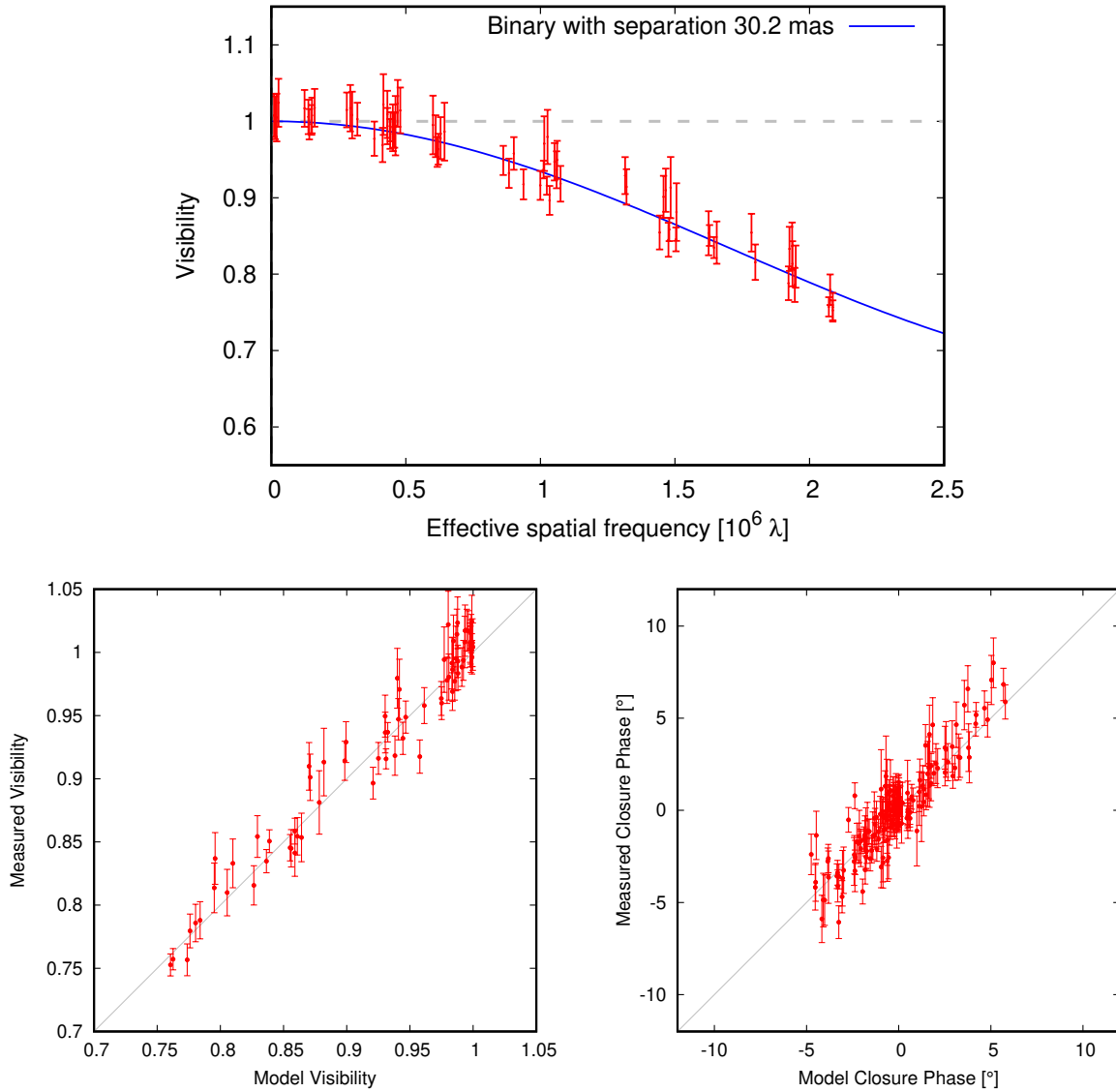


Figure S15 – NIRC2 L-band aperture masking data recorded with Keck2. Top: Visibilities plotted versus effective spatial frequency that has been projected along the best-fit (AB)-C separation vector to reveal the sinusoidal visibility modulation induced by the tertiary/circumtertiary emission. Bottom: The measured visibilities (left) and closure phases (right) plotted versus the model values.

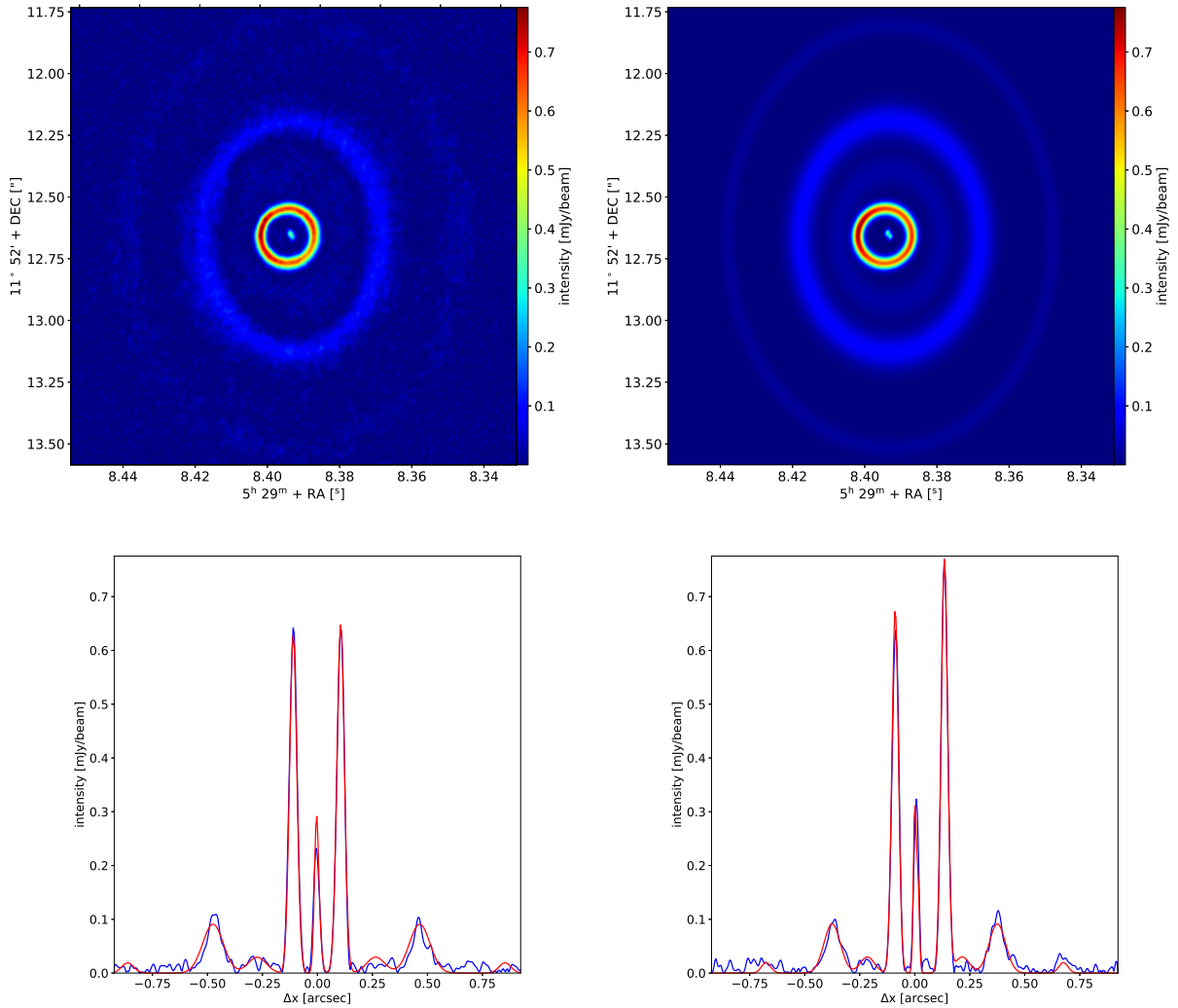


Figure S16 – Top: ALMA image (left) and synthetic image for our best-fit model (right). Bottom: Radial intensity cuts along the disk major (left) and minor axis (right), for the ALMA image (blue line) and the model (red line).

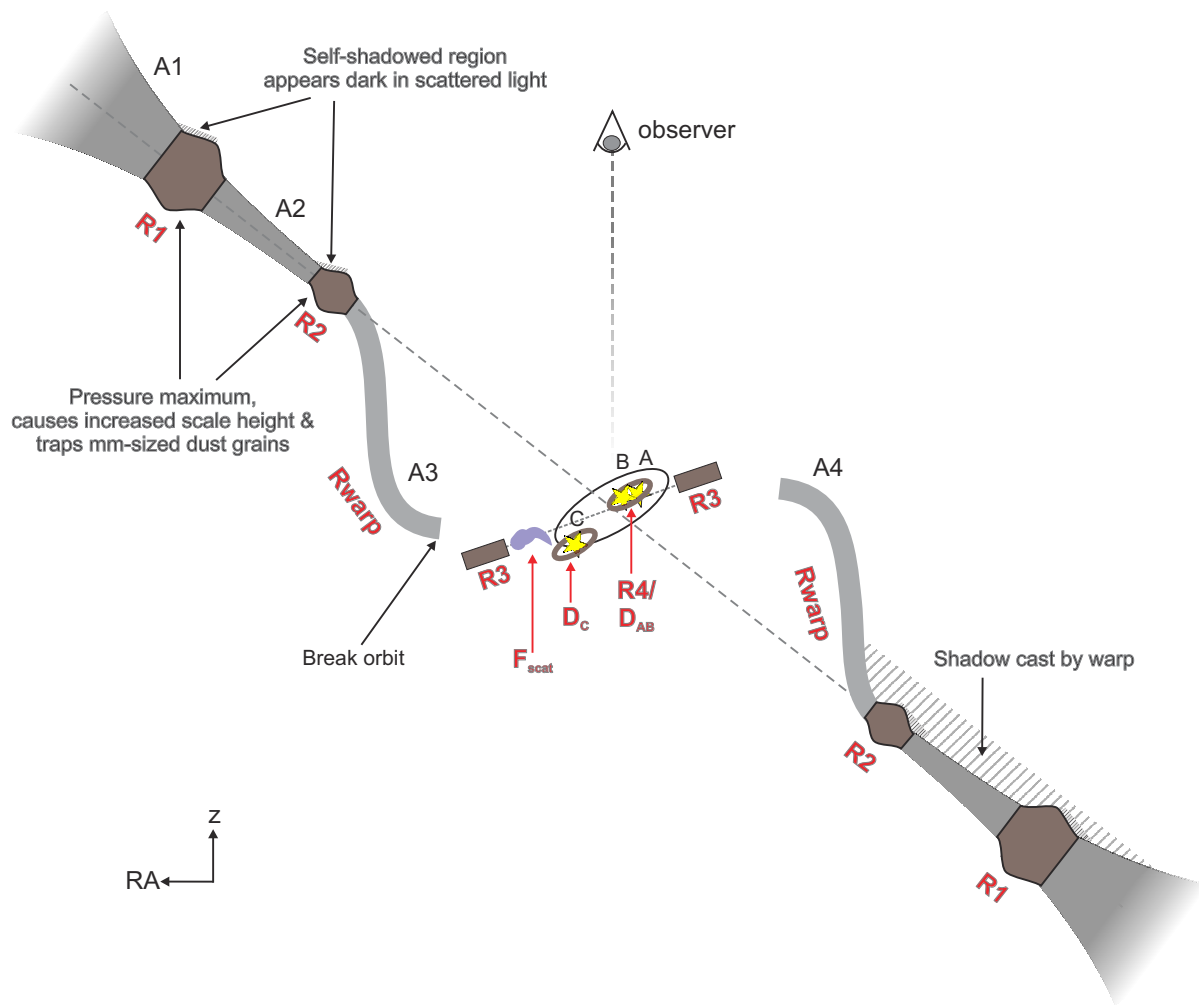


Figure S17 – Illustration of the deduced disk components and their relative viewing geometry. This sketch is not to scale.

Interactive 3D graphics (open with Acrobat Reader or Acrobat Pro to display properly)

Figure S18 – Interactive 3-dimensional graphics that illustrates the ray-tracing model and our derived disk geometry for GW Ori. Open with Acrobat Reader or Acrobat Pro to display interactive elements properly. Other viewers, such as macOS 'Preview', do not work. The default view shows the view from Earth. In order to zoom in and to see the triple star orbits, click on the plot and use a mouse up/down swipe, a mouse wheel, a trackpad 2-finger swipe gesture, or the toolbar elements. Use click+drag to rotate the system. The x-y plane defines the plane of the sky (green arrow=East; red arrow=North), while the z axis (blue arrow) points towards the observer. The coordinate system is centered on the center-of-mass of the system.

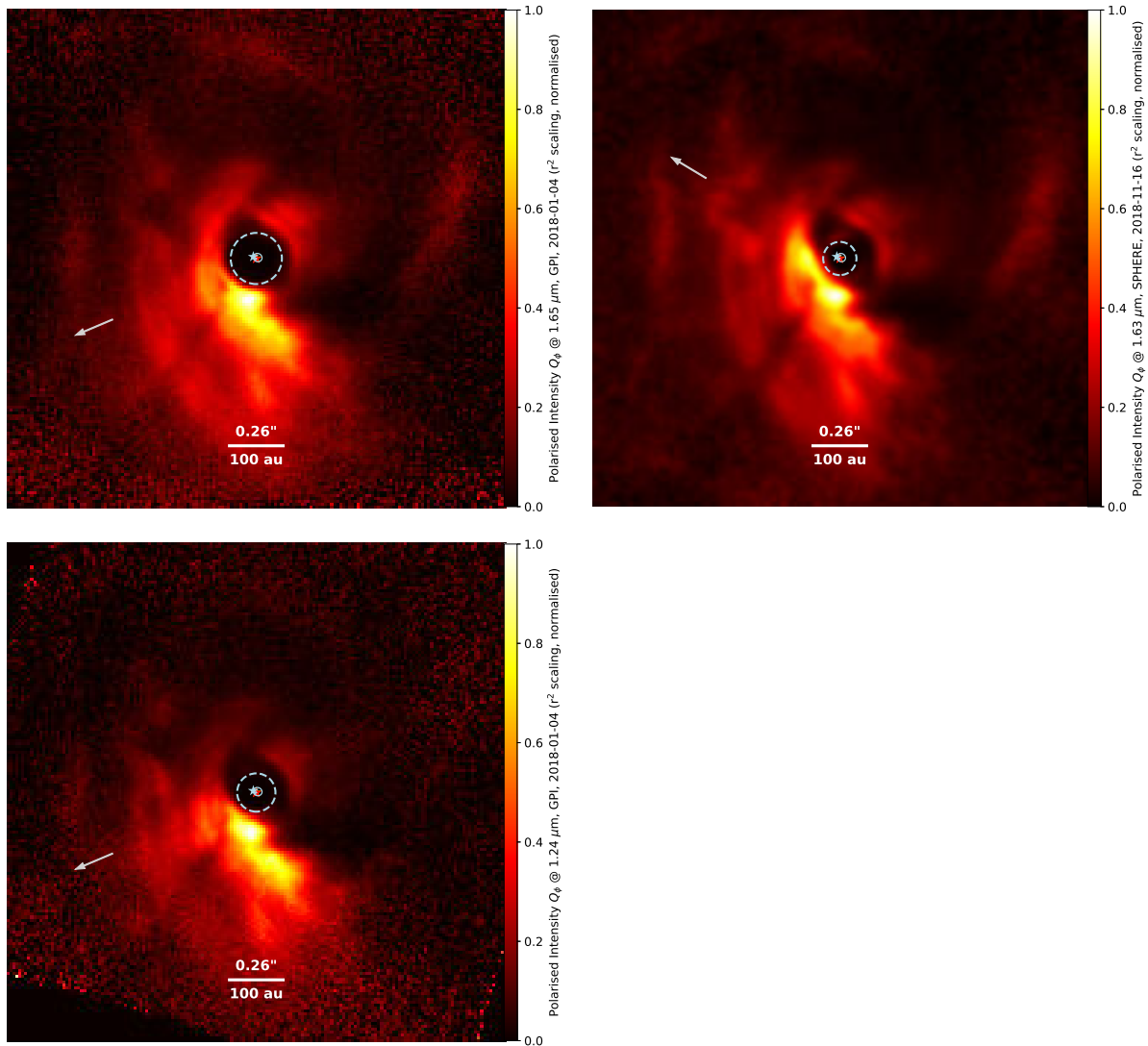


Figure S19 – Scattered-light images recorded on 2018 January 04 (left, GPI) and 2018 November 16 (right, SPHERE), plotted with  $r^2$ -scaling and normalisation to enable a direct comparison of the scattered-light geometry at the two epochs. For GPI (left row), we recorded images in H-band (top) and J-band (bottom). We include arrows that mark the direction of the tertiary at the time of the two epochs.